

AMERICAN UNIVERSITY OF BEIRUT

A HYBRID MODEL BASED ON PITCH-CATCH AND PULSE-
ECHO CONFIGURATIONS FOR OPTIMIZATION OF
PLACEMENT OF PIEZOELECTRIC WAFERS

by
KAREN JOSEPH SAAD

A thesis
submitted in partial fulfillment of the requirements
for the degree of Master of Engineering Management
to the Department of Industrial Engineering and Management
of the Maroun Semaan Faculty of Engineering & Architecture
at the American University of Beirut

Beirut, Lebanon
June 2020

AMERICAN UNIVERSITY OF BEIRUT

A HYBRID MODEL BASED ON PITCH-CATCH AND PULSE-
ECHO CONFIGURATIONS FOR OPTIMIZATION OF
PLACEMENT OF PIEZOELECTRIC WAFERS

by
KAREN JOSEPH SAAD

Approved by:



Tarhini, Hussein, Assistant Professors
Department of Industrial Engineering and Management

Advisor



Mustapha, Samir, Assistant Professors
Department of Mechanical Engineering

Member of Committee



Dr. Maddah, Bacel, Chairperson
Department of Industrial Engineering and Management

Member of Committee

Date of thesis defense: June 19, 2020

To whom it may concern,

Karen Saad has completed her thesis requirements under my supervision. I want to confirm that I am signing on the behalf of the other committee members.

Best,

*Hussein Tarhini, PhD
Assistant Professor
Department of Industrial Engineering and Management
504 Bechtel
American University of Beirut (AUB)*

A handwritten signature in black ink, appearing to be 'H. Tarhini', with a horizontal line drawn through the middle of the signature.

AMERICAN UNIVERSITY OF BEIRUT

THESIS, DISSERTATION, PROJECT RELEASE FORM

Student Name: Saad Karen Joseph
 Last First Middle

☒ Master's Thesis ☐ Master's Project ☐ Doctoral Dissertation

☒ I authorize the American University of Beirut to: (a) reproduce hard or electronic copies of my thesis, dissertation, or project; (b) include such copies in the archives and digital repositories of the University; and (c) make freely available such copies to third parties for research or educational purposes.

☐ I authorize the American University of Beirut, to: (a) reproduce hard or electronic copies of it; (b) include such copies in the archives and digital repositories of the University; and (c) make freely available such copies to third parties for research or educational purposes after:

One ---- year from the date of submission of my thesis, dissertation, or project.
Two ---- years from the date of submission of my thesis, dissertation, or project.
Three ---- years from the date of submission of my thesis, dissertation, or project.

Karen Saad

June 30, 2020

Signature

Date

ACKNOWLEDGMENTS

Special thanks are for Dr. Hussein Tarhini, and Dr. Samir Mustapha for their great help, continuous support and assistance in this research.

My recognition and gratitude are addressed to the American University of Beirut for all its financial support and for providing all the educational needs that helped me in completing my Master's degree.

AN ABSTRACT OF THE THESIS OF

Karen Joseph Saad for

Master of Engineering Management

Major: Engineering Management

Title: A Hybrid Model Based on Pitch-Catch and Pulse-Echo Configurations for Optimization of Placement of Piezoelectric Wafers

The development of Structural Health Monitoring (SHM) systems, and integration in our structures, became a necessity as it has proven to provide a robust and low-cost solution for monitoring the structural integrity, and has a better ability to predict the remaining life of structures. One of the most important aspects of SHM systems is the design and implementation of sensor networks.

This study proposes a new hybrid approach for optimizing piezoelectric (PZT) wafers on convex and non-convex structures. The developed model aims at minimizing the number of wafer elements used while ensuring a high level of coverage within the monitored area that is discretized into a set of control points. The model combines two modes of communications (pitch-catch and pulse-echo) between actuator-sensor pairs, ultimately to achieve the desired coverage with a reduced number of PZT elements.

The efficiency of the proposed model is demonstrated by simulating different geometrical shapes. Significant improvement in the coverage, reaching 34.6%, of the monitored area, was achieved when compared to the coverage provided by the preliminary solutions. The combination of the two configurations of pitch-catch and pulse-echo in the same model highly impacted the coverage in the blind zones (corners and edges) where a single configuration may not be effective.

Experimental validation was carried out to evaluate the model accuracy in damage localization within the optimized sensor networks. The results demonstrated the proficiency of the model developed in distributing the PZT wafers on the tested specimens.

CONTENTS

ACKNOWLEDGEMENTS	v
ABSTRACT.....	vi
LIST OF ILLUSTRATIONS.....	ix
LIST OF TABLES.....	xi
Chapter	
I. INTRODUCTION.....	1
II. METHODOLOGY	8
III. MODEL PARAMETERS	15
A. Experimental Setup	15
B. Dispersion Curve	16
C. Reflection Coverage	18
D. Path Coverage	20
E. Maximum Spacing Between Actuator-sensor Pair	20
IV. SIMULATED CASES	22
V. EXPERIMENTAL VALIDATION	32
A. Experimental Setup	32
B. Signal Analysis	35
C. Data Fusion and Damage Localization	38

VI. RESULTS AND DISCUSSION	43
A. Damage Detection and Localization	43
B. Single Sensing Path Analysis	46
VII. CONCLUSION AND RECOMMENDATIONS	50
REFERENCES.....	52

ILLUSTRATIONS

Figure		Page
1.	A sketch illustrating the optimization model constraints and terminology.....	9
2.	An illustration explaining the triangular inequality equations.....	11
3.	An illustration showing the model process.....	14
4.	(a) PZT wafer placement on the aluminum plate and (b) experimental setup showing the wave generator and amplifier.....	16
5.	Theoretical and experimental dispersion curves for symmetric and antisymmetric modes.....	17
6.	Amplitude versus frequency for symmetric and antisymmetric modes.....	18
7.	Experimental setup to determine pulse-echo reflection coverage.....	19
8.	Difference between healthy and damaged signals using Hilbert transform for a pulse-echo sensing path (225 kHz).....	19
9.	Experimental setup to determine pitch-catch path coverage.....	20
10.	Attenuation curve for frequency of 225 kHz.....	21
11.	(a) Preliminary solution for square plate, (b) optimized solution for square plate, (c) preliminary solution for square plate with opening, (d) optimized solution for square plate with opening, (e) preliminary solution for T-shaped plate, (f) optimized solution for T-shaped plate, (g) preliminary solution for octagon plate, and (h) optimized solution for octagon plate.....	24
12.	(a) Pitch-catch coverage for square plate, (b) pulse-echo coverage for square plate, (c) pitch-catch coverage for square plate with opening, (d) pulse-echo coverage for square plate with opening, (e) pitch-catch coverage for T-shaped plate, (f) pulse-echo coverage for T-shaped plate, (g) pitch-catch coverage for octagon plate, and (h) pulse-echo coverage for octagon plate.....	28

13.	(a) Coverage after removing each PZT wafer, (b) the normalized importance of PZT wafers, and (c) optimized PZT wafer network for square plate with an opening.....	31
14.	(a) Localizing the PZT wafers using the optimized coordinate results and (b) the optimized PZT wafer network of the square plate with an opening.....	33
15.	PZT wafer network with the damage placed according to damage case (a) 1, (b) 2, (c) 3, (d) 4, and (e) schematic showing the location of all damage cases.....	34
16.	(a) Healthy and damaged signals resulting from pulse-echo sensing path of PZT wafer 6 for damage case 2, (b) Hilbert transform of the signals, (c) difference between the two signals, and (d) Healthy and damaged signals resulting from pulse-echo sensing path of PZT wafer 1.....	36
17.	Healthy and damaged signals resulting from pitch-catch sensing path of PZT wafers (a) 7-9 and (b) 1-3 for damage case 2.....	38
18.	Damage localization on the square plate with an opening for (a) damage 1, (b) damage 2, (c) damage 3, (d) damage 4 of the optimized network, (e) the sensor network after removing some sensors, and (f) damage 2 of the network with missing sensors.....	44
19.	(a) PZT 7 pulse-echo sensing path for damage 1, (b) 7-9 pitch-catch sensing path for damage 2, (c) PZT 8 pulse-echo sensing path for damage 2, (d) 1-4 pitch-catch sensing path for damage 3, (e) PZT 1 pulse-echo sensing path for damage 3, (f) 1-8 pitch-catch sensing path for damage 4, and (g) PZT 9 pulse-echo sensing path for damage 4.....	46

TABLES

Table		Page
1.	Simulation cases for PZT wafer networks.....	26
2.	Pitch-catch and pulse-echo coverage for simulated cases.....	29
3.	Optimized locations of the PZT wafers.....	31
4.	Damage scenarios and predicted locations using excitation frequencies of 225 and 250 kHz.....	45

CHAPTER I

INTRODUCTION

SHM is one of the booming fields in engineering that monitors the state and health of the structure through continuous diagnosis. All this is achieved through a system of actuators and sensors, data processing units, and communication systems. Several studies have shown the benefit of SHM technologies in maintaining the structure by improving its safety and decreasing maintenance inspections and repair costs.^{1, 2} SHM is also a means of replacing visual inspection techniques and can guarantee the detection of certain impact damages that are hardly detectable otherwise.³

In general, operational efficiency, service life of aging assets, and reliability are all improved and increased when the SHM is successfully implemented on the structure.⁴ One of the major techniques used for damage detection are the ultrasonic methods. The importance of the latter is its enhanced flaw detection through thin and thick materials, high accuracy and sensitivity to the defect, and high-speed processing and imaging options. Accordingly, different SHM techniques were developed in accordance with Lamb-waves in shell-like structures and thin plates.^{5, 6} Because of the sensitivity of Lamb waves to several damage types as well as their major propagation properties (low dispersion and attenuation), Lamb-waves have been of high interest in the field of damage detection recently.^{7, 8} Knowing that PZTs have a special feature which is the electro-mechanical coupling, this makes them appropriate for use in passive^{9, 10} and active sensing^{11, 12} as both sensors and actuators. The challenge is to determine the number of sensors required as well as the most optimal locations to place them on a structure in order to identify its characteristics in the best and most efficient

manner. Several methods have been proposed for sensor network optimization and are widely found in the literature. Many researches have determined the optimal sensor layout based on a given number of sensors. However, this assumption of having the number of sensors a priori and fed to the system is not a practical nor a realistic one.¹³

An effective method has been presented by Tarhini et al.¹⁴ using a mixed integer nonlinear program (MINLP) for the optimization of PZT wafer networks in SHM. A mathematical programming language (AMPL) was used, and the objective function aimed at maximizing the number of covered control points. A point is considered as covered if a user-defined number of sensing paths pass through it. Experimental validation showed satisfactory coverage results for the area studied with high accuracy in damage detection. For Thiene et al.,¹⁵ they tackled the optimal placement of sensors based on maximum area coverage (MAC) using the physical properties of Lamb waves and geometrical complexities. A major advantage of this method is that it does not rely on probability of detection (POD) for every sensor combination which is more expensive. Using a fixed number of transducers and GA, a fitness function which does not rely on damage parameters such as location, severity, and type was minimized to result in the locations of optimal sensors. Salmanpour et al.¹⁶ considered irregular shapes, defective transducers, and stiffeners while finding an optimized transducer layout using also GA. Two suboptimal layouts were compared to the optimized one to determine the effectiveness of the optimization strategy by using the finite element analysis-simulated signals that output the predicted damage maps. It was determined that the optimized layout showed more accurate results concerning detection, false peak regions because of waves reflected by the boundaries, and low noise levels.

Zhou et al.⁴ presented a new approach concerning the probability-based diagnostic imaging (PDI). Using both pitch-catch and pulse-echo configurations in an active sensor network, hybrid signal features were determined. A new concept, ‘virtual sensing’, was used to introduce virtually more sensing paths without adding more sensors physically. Hybrid image fusion was shown to enhance damage detection by reducing inaccurate perceptions and noise from individual sensing paths. A similar study relying on PDI in an active sensor network with pulse-echo configuration focused on determining the orientation, shape, size, and location of the damage.¹⁷ Wang et al.¹⁸ also adopted an algorithm that is based on correlation analysis for localizing damages in aluminum plates. Applying the Shannon entropy optimization, the most relevant and optimal mother wavelet for signal processing was calibrated. As for Zhou, virtual sensing was used to enhance the algorithm’s performance. In the context of PDI, Wu et al.¹⁹ determined empirically the parameters including the frequency, the elliptical size of the distribution area, the selection of certain damage index, and the sensing paths of the network. This results in limitation when applying the method for real-life damage localization practices. To eliminate the effect of selecting the frequency, multiple frequencies were considered in a fusion image approach. The robustness of this fusion was evaluated in a histogram plot showing the effect of the fusion as compared to the individual behavior. The conclusion showed the decrease in the localization error while removing the intrusion between the frequency selection and other factors.

According to Worden et al.,²⁰ they used combinatorial optimization methods and neural networks to detect and classify faults in a cantilever plate. The faults are represented by the removal of small groups of elements. The methods used to determine an optimized layout of sensors include simulated annealing (SA), GA, and iterative

insertion and deletion. Each one alone has shown advantageous results as well as hybrid schemes such as combining GA and SA. For the iterative method, it starts by placing 20 sensors and removing one sensor after the other which affect the coverage the least. For the SA method, the probability of misclassification was assigned to be the objective function. A similar approach was proposed by Mallardo et al.²¹ based on GA for passive sensing. Algorithms for optimizing passive sensing networks use fitness functions based on probability of detection (POD). The evaluation of the considered fitness function is the main difference between active and passive sensing networks used for optimization.²² In the context of POD, receiver operating characteristic curves was investigated in the assessment and detection of damage in metallic structures.²³

Other approaches were used such as Bayes risk by Flynn et al.^{24, 25} in order to determine an optimal sensor network for damage detection through active sensing. The structure was divided into regions, and each one was assigned set of costs for the different possible scenarios of the local detection and a priori probability of damage. The measure of consequences of a detection event is the cost. Bayes risk is taken as the total expected costs of detection in all the regions. This was the fitness function of GA to determine the optimal sensor locations. Staszewski et al.²⁶ proposed to obtain the objective function from ANN for damage detection. In order to train the network, extensive damage scenarios were studied. In addition, Guo et al.²⁷ studied a metallic truss structure to determine the optimal sensor location using an improved GA. Sun et al.²⁸ considered an innovative approach for an optimal sensor placement for three kinds of sensors (PZT, accelerometers, and Fiber Brag Gauges sensors). For improving the damage detection method, integration of multi-type sensor data was applied along with a sensitivity-based objective function while considering the boundary effects and the

uncertainties from the surrounding environment. According to Croxford et al.,²⁹ quantitative and qualitative investigation on the performance of multiple sensor pairs was done to determine the effect of triangle, rectangular, trapezoidal, and other sensor patterns on damage detection using guided waves in aluminum plates. The results showed that there is no unique optimal sensor configuration that would be dependent on a certain damage to be detected. In addition, a square or hexagonal configuration showed an optimum performance for several defect scenarios. Likewise, Malinowski et al. have determined the effect of transducer configuration pattern in two studies.^{30, 31}

SHM applications that are based on Lamb waves are showing increased interest in imaging techniques. The aim behind these imaging results are to present the health status of the structure under inspection through images that can be easily interpreted and analyzed. This mode of application reduces the reliance on individual operators that present subjective interpretation of signals. Image reconstruction requires a dense wave path while using traditional wave approaches that are symbolized by Lamb wave tomography.^{32, 33} This leads to the use of many transducers or the rotation of the inspected object using small increments. A study done by Su et al.³⁴ explored several data fusion schemes which are the disjunctive, conjunctive, and compromise fusion. They tested the efficiency of each in estimating mono- and multi-delamination in composite structure made of carbon fiber-epoxy. Another study by Su et al.³⁵ investigated the development of an imaging technique with Lamb waves. It also presented the ability to detect structural damage using the probability of availability of damage for all grid points in the area under study. The time of flight that resulted from the captured Lamb wave signals of the corresponding sensors in an active sensor network contributed in the perception of the damage localization. Using an arithmetic

algorithm, all these perceptions were fused together. In addition, damage localization was thoroughly investigated for simple plates and pipes^{36, 37} in the application of guided wave signal processing. In the context of optimal sensor placement, Lee et al.³⁸ aimed to maximize the interaction of Lamb waves with a defect in order to find the optimal locations of sensors. Using the local interaction simulation approach, this method is experimented with a rectangular damage and a fatigue crack on an aluminum plate and involved numerical simulations of Lamb wave interactions. It presents the areas where it is most convenient to place sensors rather than giving exact locations for the optimal sensors. Fendzi et al.³⁹ focused on determining optimal sensors placement in composite plates for enhancing the localization and detection of damages. The novel approach in this study was the use of the characteristics and physical phenomenon of Lamb wave propagation as well as optical rays to find sensor placement. GA method was used to solve the optimization part, and a ray tracing approach was used to evaluate the objective function that should be maximized. Geometric Dilution of Precision (GDOP) was introduced in order to account for the spatial distribution of the sensor location in the objective function.

In this study, a novel model is proposed to determine the optimal sensor locations which is an improved and upgraded version of that proposed by Ismail et al.⁴⁰ First, the objective function starts by maximizing the number of control points covered within the area studied while using the least number of PZT wafers. A GA is adopted in this study since it is shown to be effective in sensor network optimization. Then, the path coverage limits for both mechanisms are determined through experimentation on an aluminum plate. Afterwards, different geometries are simulated to obtain the optimized PZT wafer network and to demonstrate the effectiveness of the proposed

model. The advantage of combining both configurations together is determined through investigating the contribution of each mechanism alone. Furthermore, the latter is validated through investigating the precision in detecting the damage location for the optimized PZT wafer network using both coverage mechanisms.

CHAPTER II

METHODOLOGY

Using a predefined and finite set of control points, the aim is to maximize their coverage through the proposed optimization algorithm. The user chooses a coverage level (n) which defines the number of sensing paths that should cover a control point in order to consider it as covered. According to Huang and Tseng,⁴¹ at least three sensing paths are required ($n = 3$) for accurate damage localization based on triangulation protocols. The coverage of a control point is provided by the superposition of pitch-catch and pulse-echo sensing paths passing through it. The constraints that are imposed on the model include the number of available PZT wafers (N) and the geometry of the plate which is defined as a polygon with a determined number of vertices. A minimum distance between the PZTs that are functioning through either pitch-catch or pulse-echo ($d_{\min(PC)} = d_{\min(PE)} = 30$ mm) were considered to prevent the concentration of PZTs in the same location. In addition, other constraints that are specific to the detection mechanism used are the following:

- For the pitch-catch configuration, a sensing path formed by any pair of PZT wafers covers a control point if its distance from the centerline of the sensing path is within the path coverage distance (z). To ensure the sensing paths are not collinear, the angle between two paths is constrained by a minimum ($\alpha_{\min} = 10^\circ$). A maximum distance between an actuator-sensor pair is set in order to account for the attenuation of the wave signal ($d_{eff(PC)}$).
- For the PZTs providing coverage through the pulse-echo mechanism, a maximum and a minimum distance was considered from the PZT wafer

which is acting as the center of the circular path formed ($d_{effmax}(PE)$ and

$d_{effmin}(PE)$).

Note that these model parameters are determined through experimentation on an aluminum plate that is discussed later. Although Thiene et al.¹⁵ used predefined finite locations for the optimized PZT wafers, the location of the PZTs were considered as continuous variables in this study. Figure 1 shows all the constraints and model terminologies as discussed previously.

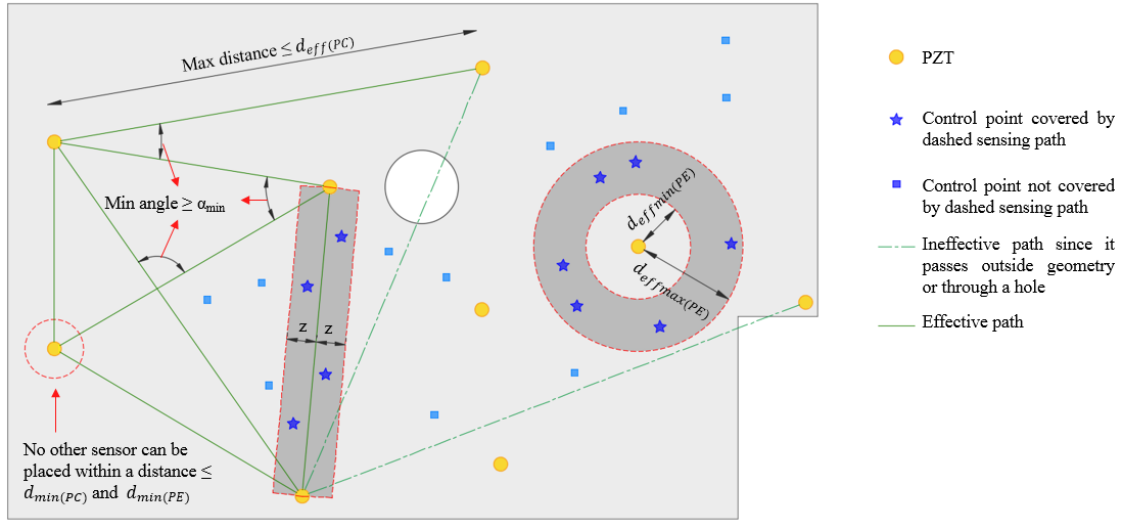


Figure 1. A sketch illustrating the optimization model constraints and terminology

Model:

The problem is summarized in equations 1 through 14 as follows:

$$\max \sum_{k \in K} C_k \quad (1)$$

$$d_{ij}^2 = (x_i - x_j)^2 + (y_i - y_j)^2 \quad (2)$$

$$d_{ik}^2 = (x_i - x_k)^2 + (y_i - y_k)^2 \quad (3)$$

$$d_{ijk} = \frac{|(y_j - y_i) \times x_k - (x_j - x_i) \times y_k + x_j \times y_i - y_j \times x_i|}{\sqrt{(y_j - y_i)^2 + (x_j - x_i)^2}} \quad (4)$$

$$C_{ijk} = 0 \text{ if } d_{ijk} > z \quad (5)$$

$$C_{ijk} = 0 \text{ if } d_{ik} > d_{ij} \quad (6)$$

$$C_{ijk} = 0 \text{ if } d_{jk} > d_{ij} \quad (7)$$

$$C_{ijk} = 0 \text{ if } d_{ij} > d_{eff(pitch-catch)} \quad (8)$$

$$C_{ik} = 0 \text{ if } d_{ik} \geq d_{effmax(pulse-echo)} \quad (9)$$

$$C_{ik} = 0 \text{ if } d_{ik} \leq d_{effmin(pulse-echo)} \quad (10)$$

$$C_k = 0 \text{ if } (\sum_{i \in N} \sum_{j \in N} C_{ijk}) + (\sum_{i \in N} C_{ik}) < n \quad (11)$$

$$C_{i_1 j_1 k} + C_{i_2 j_2 k} \leq 1 \text{ if } \left| \frac{(x_{j_1} - x_{i_1})(x_{j_2} - x_{i_2}) + (y_{j_1} - y_{i_1})(y_{j_2} - y_{i_2})}{\sqrt{((x_{j_1} - x_{i_1})^2 + (y_{j_1} - y_{i_1})^2)((x_{j_2} - x_{i_2})^2 + (y_{j_2} - y_{i_2})^2)}} \right| > \cos \alpha_{min} \quad (12)$$

$$d_{ij} \geq \max(d_{min(pitch\ catch)}, d_{min(pulse-echo)}) \quad (13)$$

$$(x_i, y_i) \in X \quad (14)$$

Equation (1) shows the objective function which is to maximize the total number of covered control points. If C_k is 1, it means that control point k is covered with respect to the previously defined coverage level. The computation of the distance between two PZT wafers and between a PZT wafer and a control point k are shown in equations (2) and (3) respectively. Using the formula of the distance between a point and a straight line, equation (4) computes the distance between a control point k and a sensing path (i, j) .

Concerning the pitch-catch configuration, equation (5) states that for a control point k to be covered by a path (i, j) , d_{ijk} should be less than the coverage distance z . In addition, the triangular inequality equations were used in equations (6) and (7) to ensure the coverage of a control point if it falls in the rectangular range of the sensing path of

an actuator-sensor pair. Referring to Figure 2, control point k is not covered by path (i, j) in this case since $d_{ik} > d_{ij}$. Because wave attenuates at long distances, equation (8) disregards all actuator-sensor pairs whose path is longer than $d_{eff(PC)}$.

Concerning the pulse-echo configuration, equation (9) disregards all control points located at a distance farther than $d_{effmax(PE)}$ from the PZT wafer. Equation (10) disregards all control points located at a distance which is less than $d_{effmin(PE)}$ from the PZT wafer.

Equation (11) defines whether the coverage level n is reached for control point k. If it is covered by n or more sensing paths from either the pitch-catch or the pulse-echo configuration, then this control point is covered. To make sure the pitch-catch sensing paths are not collinear, equation (12) constraints the minimum angle between any two paths to be at least α_{min} . Equation (13) ensures the PZT wafers to be separated from each other by a distance which is the maximum between the minimum distances required by the pitch-catch and pulse-echo configurations to prevent their concentration in the same location. Equation (14) defines X which is the set of all points lying in the plates' geometry. The PZT wafer coordinates (x_i, y_i) could be any point of this set.

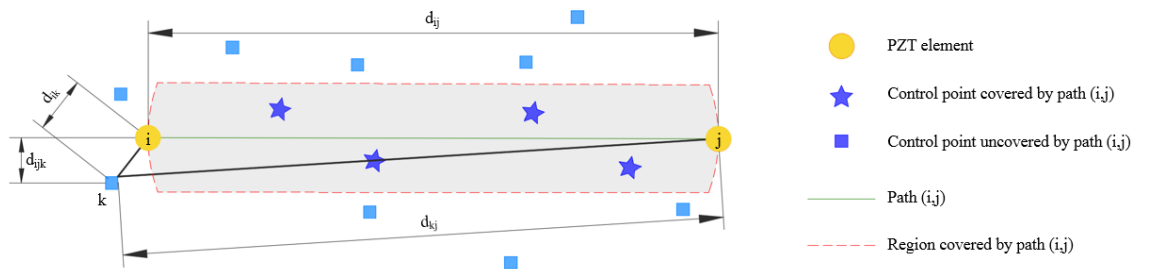


Figure 2. An illustration explaining the triangular inequality equations

Since the problem is a non-convex one, it is not possible to determine whether the problem has a local or global optimum solution. Therefore, a program was

developed that generates a preliminary solution which will be fed to the optimization algorithm in order to reduce the possibility of being stuck on a bad local maximum.

The proposed model was solved using GA which is an optimization tool. The latter uses a heuristic approach to evolve solutions that solves the given problem. A population of chromosomes are used as solutions where each has a fitness value obtained from the fitness function, a measure to evaluate the effectiveness of the solution.⁴² In this case, the aim is to maximize the fitness function which is represented as the percentage coverage of the control points. A chromosome has number of genes equal to double the number of PZT wafers where each gene represents either an x or a y coordinate of a PZT. The algorithm starts with an initial population of chromosomes that is improved through selection and recombination to produce the next generation. For the selection process, chromosomes with higher fitness values are more likely to be selected to generate more highly fit solutions. For the recombination, the mixing of genetic material is the result of recombining the selected chromosomes through crossover and mutation. The algorithm terminates when the solution converges to a satisfactory fitness level, when the maximum number of generations is reached, or when further generations show no improvement in the fitness value. The heuristic crossover function along with the gaussian mutation were used in the MATLAB GA function.⁴³

The following steps are followed to find the optimal PZT wafer locations:

- The geometry is first discretized into control points, and the number of PZTs used to start the analysis is determined as the midpoint of the range provided by the user.
- The preliminary solution is configured either by distributing the chosen number of PZT wafers evenly in the geometry within a grid pattern or

uniformly along the borders of the plate geometry. Afterwards, the effective sensing paths are determined for the preliminary sensor network. This consists of removing the pitch-catch paths whose centerline (line joining the two PZT wafers corresponding to this path) is obstructed by any discontinuity or an edge for instance. For the pulse-echo sensing paths, this effectiveness is evaluated at the level of each control point in the area studied. If the line joining this control point and the PZT wafer is not cut by any obstruction, then the sensing path is considered as effective for this point and may be considered for coverage later. The coverage of the preliminary layout is computed.

- This solution is fed to the GA which will result in the optimized layout consisting of N PZT wafers. The effectiveness of the sensing paths is recomputed for the new optimized PZT network as well as its coverage.
- This coverage is compared to the desired predefined coverage (95% for this study). If the coverage is above the desired one, the upper bound on the number of PZTs becomes N . However, if the coverage is below the desired one, the lower bound on the number of PZTs becomes N . The process is repeated with the new N as the midpoint of the new range.

The algorithm runs automatically for multiple times while changing the number of PZTs (N) and calculating its corresponding coverage during each scenario. Once the algorithm reaches a coverage which is equal to or above a desired predefined coverage (95% for this study) with the least number of PZTs, the solution is returned. Figure 3 explains the process that is followed by the model.

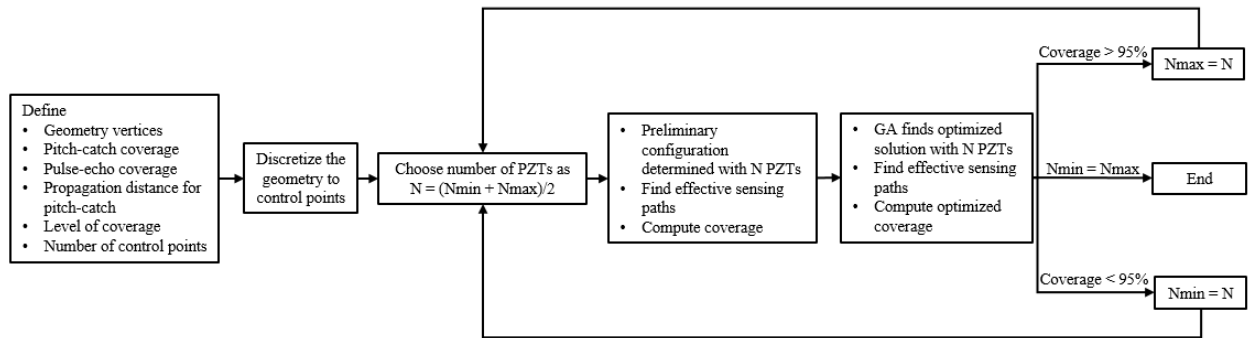


Figure 3. An illustration showing the model process

CHAPTER 3

MODEL PARAMETERS

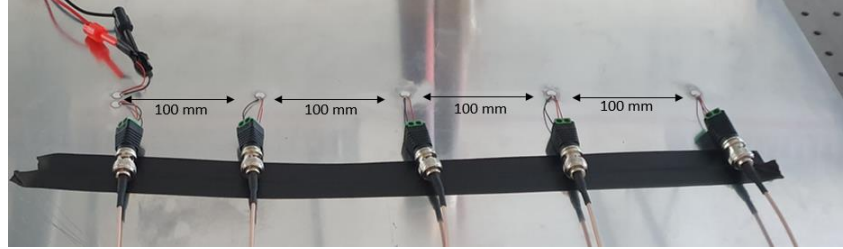
Sensing path parameters that are determined through experimentation on an aluminum plate are the following:

- Maximum and minimum detection length for pulse-echo sensing path ($d_{\text{effmax(PE)}}$ and $d_{\text{effmin(PE)}}$)
- Path coverage for pitch-catch sensing path (z) (normal distance from path centerline)
- Maximum spacing between the actuator-sensor pair ($d_{\text{eff(PC)}}$)

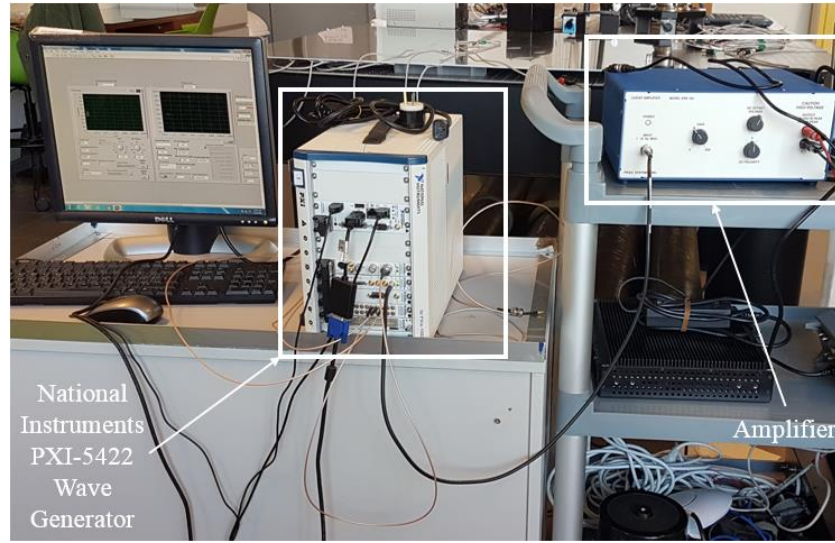
A. Experiment setup

An Aluminum 1050 plate measuring $1000 \times 1000 \text{ mm}^2$ was used with a thickness of 3 mm. The PZTs (6 mm diameter, 0.5 mm thickness) used have wrapped electrodes (PI Ceramics, Lederhose, Germany). Due to hardware limitation, two PZT wafers were mounted in the middle of the plate with a 1 cm distance between them to function as a single PZT wafer that detects damage through reflection (pulse-echo). One acts as an actuator, and the other as a receiving sensor. Four other PZT wafers were placed on a straight line with distances of 100 mm, 200 mm, 300 mm, and 400 mm from the actuator as shown in Figure 4 (a). A wave generator (NI PXI-5422) was used to generate 5-cycle Hanning-windowed tone bursts sampled at a rate of 20 MSa/s as shown in Figure 4 (b). Before feeding the signal to the actuator PZT, it was amplified to 91 volts peak-to-peak voltage using an amplifier (EPA-104 Linear Amplifier, Piezo Systems Inc.). One PZT is functioning as the actuator that generates the wave signal

while the other PZT is acting as a sensor that receives it. The captured wave signal was done using the NI PXIe-2593 multiplexer and the NI PXIe-5122 digitizer.



(a)



(b)

Figure 4. (a) PZT wafer placement on the aluminum plate and (b) experimental setup showing the wave generator and amplifier

B. Dispersion Curve

Using a pitch-catch sensing path, signals were recorded for several excitation frequencies. The velocities of both modes (antisymmetric A_0 and symmetric S_0 mode) were calculated using the highest peaks of the recorded signals. The distance between the PZT pair is divided by the time at which the peak occurs to result in the corresponding velocity. Comparing these experimental velocities to those obtained from Wavescope (LAMSS) for Aluminum 1050, Figure 5 displays the results for both modes. It is clearly shown how close both observations are to the theoretical ones.

The amplitudes of the signals were plotted with respect to the excitation frequencies for A_0 and S_0 modes (Figure 6). Since the amplitude of the A_0 mode reached the highest values for the range of frequencies between 210 and 310 kHz, the frequency to be used in this study is expected to fall in that range. The exact frequency is determined afterwards when investigating which frequencies show the reflection peak clearly for the signals detected through the pulse-echo configuration.

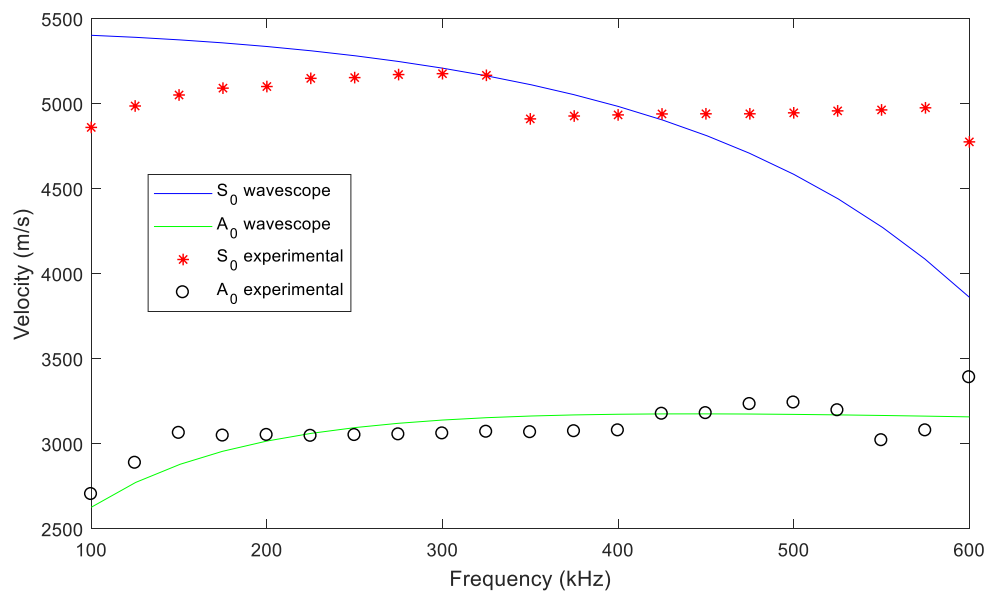


Figure 5. Theoretical and experimental dispersion curves for symmetric and antisymmetric modes

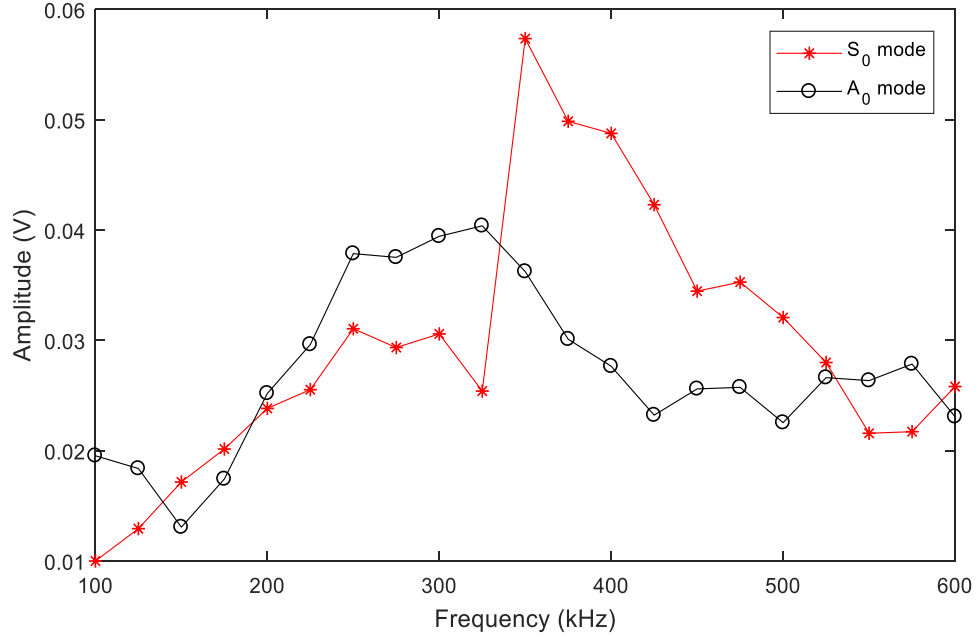


Figure 6. Amplitude versus frequency for symmetric and antisymmetric modes

C. Reflection Coverage

This experiment was done using the actuator-sensor pair placed 1 cm apart. A 50×50×50 mm octagon-based prism steel block was used as an artificial damage by gluing it to the plate using super glue. The steel block was placed at an initial distance of 7.5 cm from the PZT pair. It was then moved on a straight line passing through the PZT pair with increments of 25 mm until reaching a final distance of 175 mm from the pair as shown in Figure 7, and the reflected signal was recorded for each case.

After analyzing the wave signals for different frequencies, the damage reflected fundamental order A_0 mode was observed clearly with excitation frequencies of 225 and 250 kHz. Thus, these frequencies were selected for this study where the A_0 mode dominates over the S_0 mode. Referring to Figure 8, the difference between the baseline healthy signal and the damage reflected one was plotted using the Hilbert transform for each damage case. By investigating the reflection peaks, reflection via

pulse-echo was observed explicitly for the first four damage cases. Thus, the coverage is compared to a donut-shape with a minimum detection radial distance of 75 mm

($d_{effmin(PE)}$) from the PZT pair up to a maximum distance of 150 mm ($d_{effmax(PE)}$).

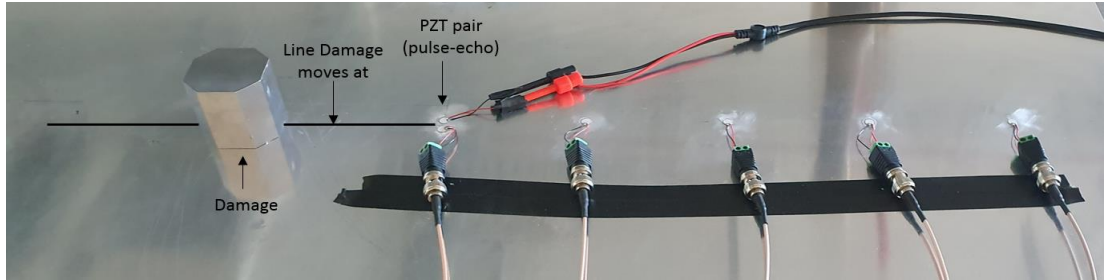


Figure 7. Experimental setup to determine pulse-echo reflection coverage

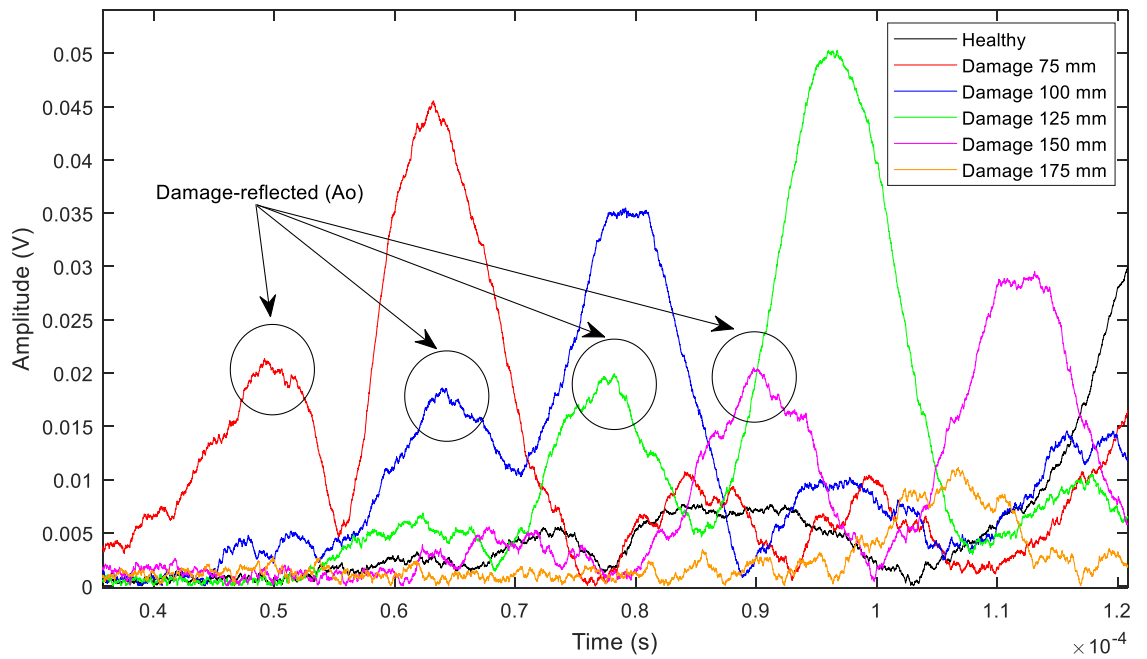


Figure 8. Difference between healthy and damaged signals using Hilbert transform for a pulse-echo sensing path (225 kHz)

D. Path Coverage

For this experiment, the steel block was first fixed to the plate at the centerline of the pitch-catch sensing path. Then, the damage was moved on the line perpendicular to the centerline of the path with increments of 1 cm as shown in Figure 9.

The wave signals (amplitude versus time) for each case were graphed on top of each other along with the healthy signal which represents the case with no damage on the plate. The case with the farthest distance between the damage and the path centerline up until which the amplitude of its signal remains below that of the healthy one was considered as the path coverage (z). In this experiment, it was found to be 50 mm from each side of the centerline; thus, a total coverage of 100 mm is considered.

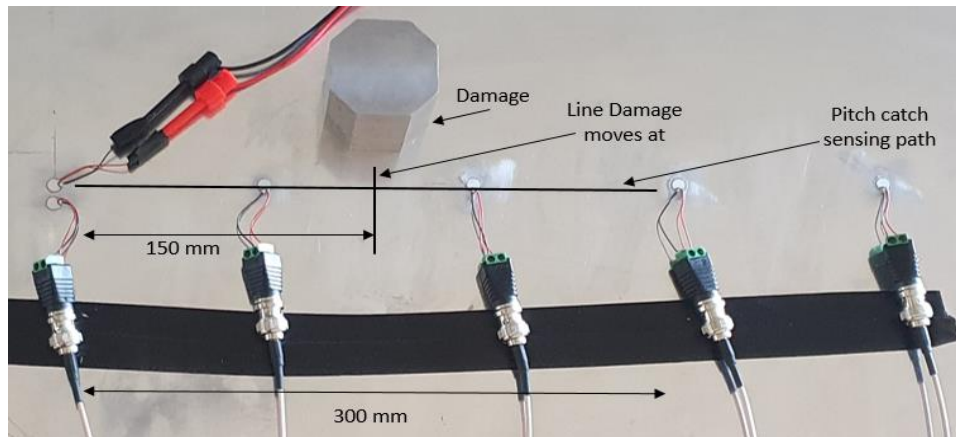


Figure 9. Experimental setup to determine pitch-catch path coverage

E. Maximum Spacing between the Actuator-sensor Pair

In this experiment, the PZT placed at the center of the plate acted as the actuator, and the four other PZTs that were placed on a straight line acted as the receiving sensors. The actuator was excited at different frequencies from 225 to 450 kHz with increments of 25 kHz.

To determine the maximum effective spacing between the actuator-sensor pair, the attenuation of the wave amplitude with respect to the distances between the pairs is

analyzed. This attenuation is due to the loss in the signal's energy when the wave propagates in the medium. This is important in order to determine the signal's strength with respect to the distance traveled.

A graph showing the normalized amplitude of the first peak of the wave signal captured from each sensor with respect to the distance of the sensor to the actuator is represented in Figure 10 (square dots). A logarithmic curve was fitted to the four graphed points. The distance at which the highest amplitude of the wave signal reaches around 20% of its value is taken as the maximum spacing ($d_{eff(PC)}$). In this case, the maximum length was found to be around 800 mm.

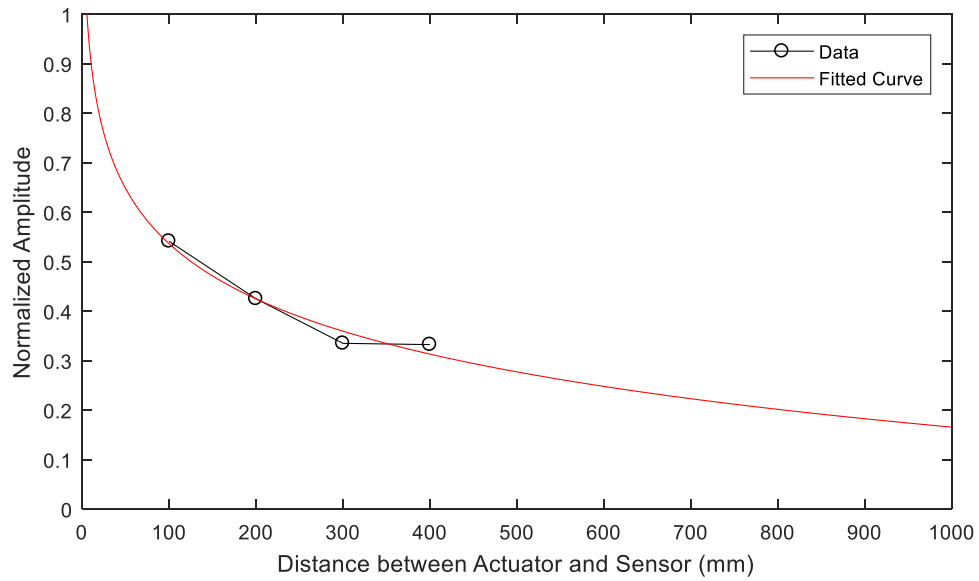


Figure 10. Attenuation curve for frequency of 225 kHz

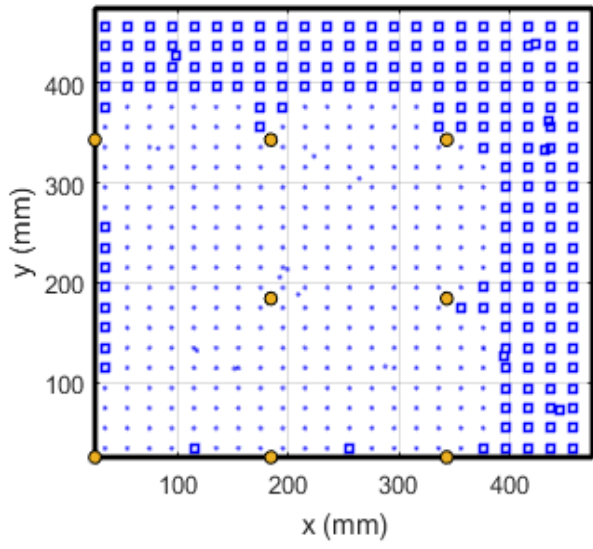
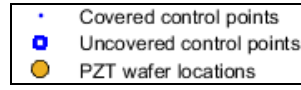
CHAPTER 4

SIMULATED CASES

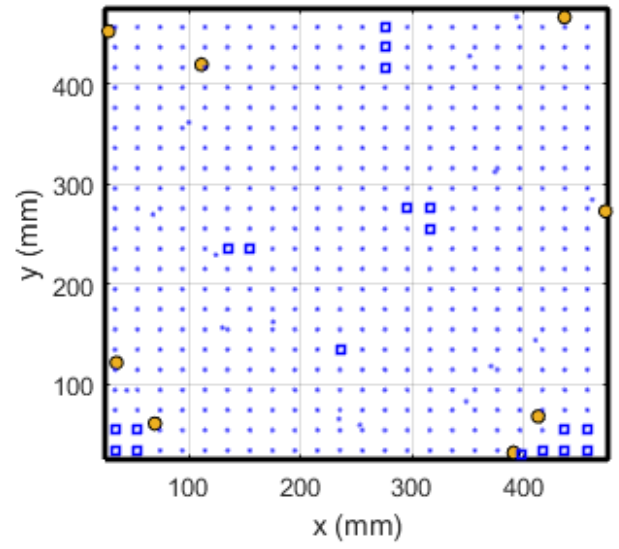
To demonstrate the effectiveness of the proposed model, several simulated cases were considered including a square plate, a square with an opening, a T-section, and an octagon plate. The user defined parameter n is chosen to have a level 3 ($n = 3$) optimization coverage for the cases studied. The primary objective of this section is to show the strength of the proposed model in localizing PZT wafers along different geometrical shapes with different boundaries. The coverage detection method for these cases considers both pitch-catch and pulse-echo mechanism.

Figure 11 shows the preliminary and the optimized solutions of PZT wafer networks resulting from the proposed model for the considered cases. The control points are distributed randomly over the geometry to cover the whole plate. The covered control points are represented as a blue dot whereas the uncovered ones are represented as a blue square. The number of sensors is the minimum N that can be reached during the optimization process for a coverage of at least 95%. The preliminary layout of all the cases considered a grid distribution pattern for the PZT wafers inside the geometry considered. For the first simulated case which is the square plate, the optimization algorithm resulted in a minimum number of PZT wafers of $N = 8$ that are required to achieve a coverage of 96.4% using 500 control points. This shows a great improvement while comparing it to the initial PZT wafer network which resulted in a 61.8% of preliminary coverage for the same number of PZT wafers (Figure 11 a-b). Notice how the PZTs were redistributed along the sides in order to benefit from the 800 mm pitch-catch sensing path by including as much as possible of control points in it.

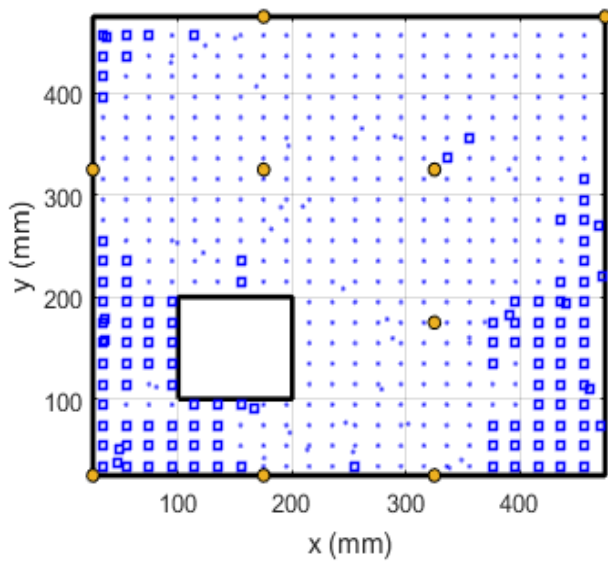
For the case of the square plate with an opening, the preliminary coverage was 76.2% compared to the optimized coverage which achieved a 96% coverage for 9 PZT wafers in both cases (Figure 11 c-d). It is interesting to note that for the initial PZT network layout, the lower left corner area next to the opening was not covered. However, for the optimized sensor network, a PZT wafer migrated to that area thus providing coverage for the control points nearby. The T-shaped plate showed an initial coverage of 77% and an optimized coverage of 96.25% for 8 PZT wafers (Figure 11 e-f) resulting in a 19.25% improvement. The preliminary and optimized coverages for the octagon plate are 83% and 97.25% respectively for 9 PZT wafers (Figure 11 g-h). As shown in Figure 11 (d) and (f), more PZT wafers are moving towards the inner of the plate than being placed across the boundaries (which is more the case of Figure 11 (b) and (h)) because of the discontinuities of the opening and the rough edges. In general, after observing all the cases, the optimized PZT wafer network provided a higher coverage as compared to the preliminary PZT network while using the same number of PZT wafers. Table 1 summarizes the initial and optimized coverage percentages for the four plates while mentioning the number of PZT wafers used in each.



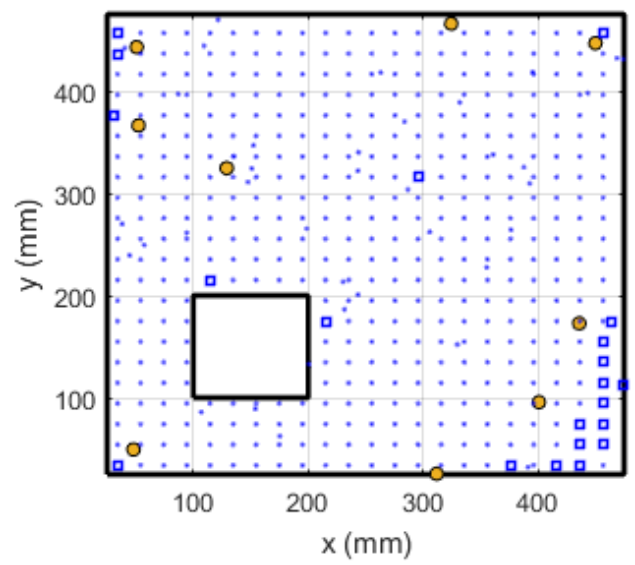
(a)



(b)



(c)



(d)

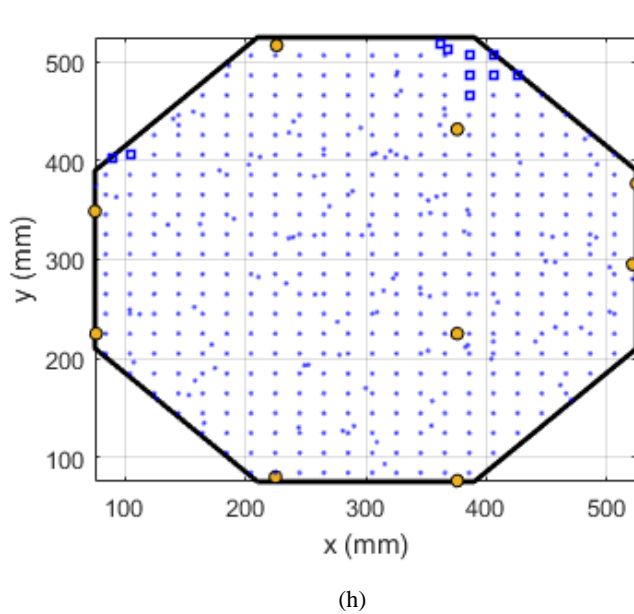
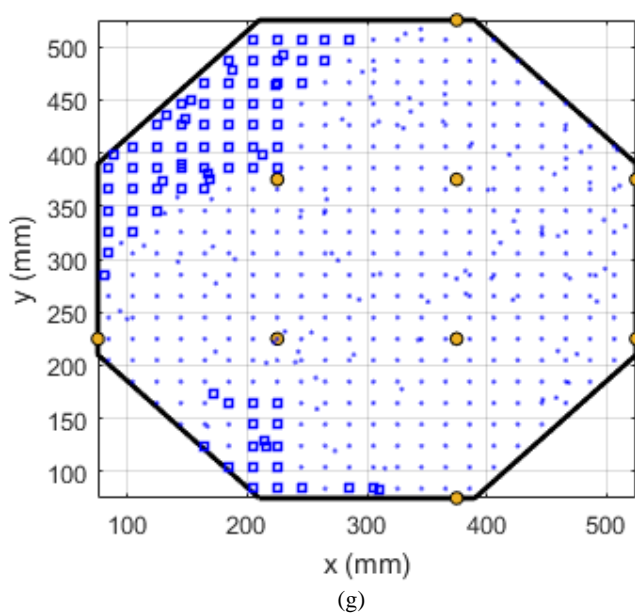
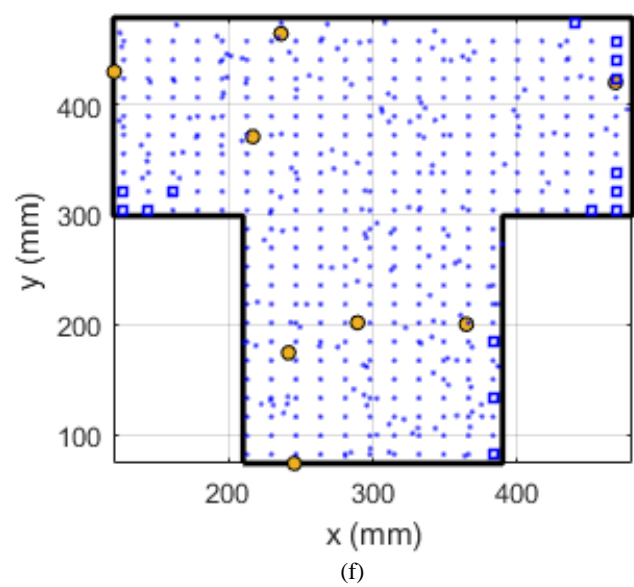
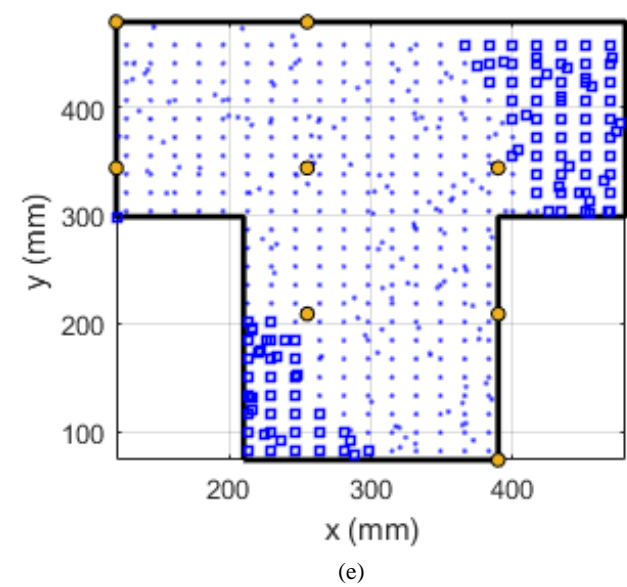


Figure 11. (a) Preliminary solution for square plate, (b) optimized solution for square plate, (c) preliminary solution for square plate with opening, (d) optimized solution for square plate with opening, (e) preliminary solution for T-shaped plate, (f) optimized solution for T-shaped plate, (g) preliminary solution for octagon plate, and (h) optimized solution for octagon plate

Table 1. Simulation cases for PZT wafer networks

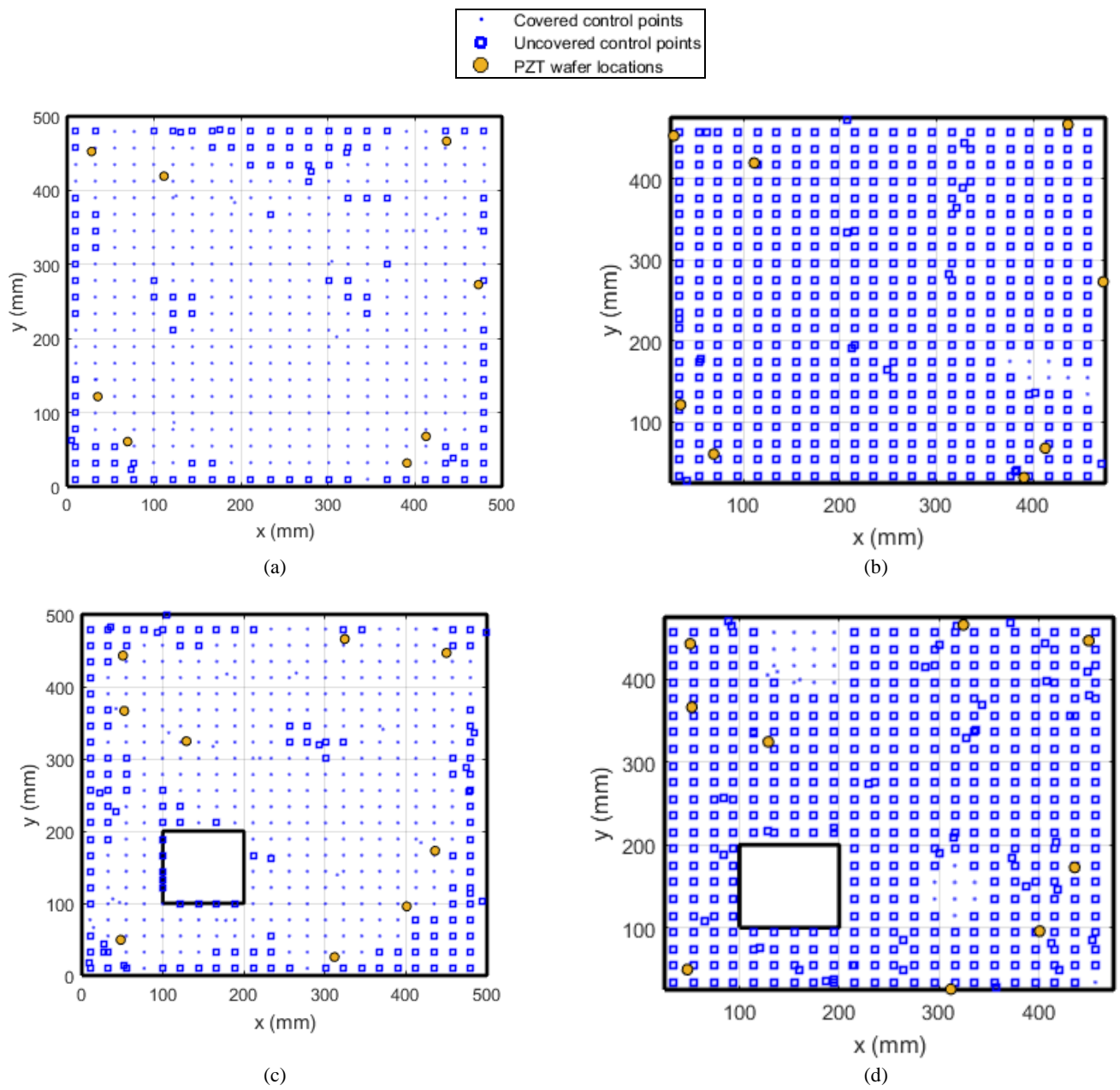
Case	PZT wafers	Initial Solution Coverage (%)	Optimized Coverage (%)
Square	8	61.8	96.4
Square with opening	9	76.2	96
T-shape	8	77	96.25
Octagon	9	83	97.25

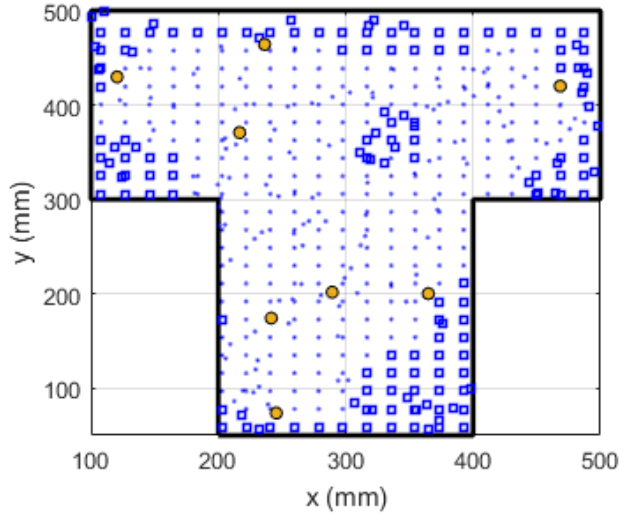
The coverage method used for the optimized PZT wafer network is further investigated in order to determine the contribution of each of the pulse-echo and pitch-catch mechanisms in covering control points. The aim behind this analysis is to show the advantage resulting from the combination of both mechanisms together as compared to the case where each mechanism is used solely. Consequently, three scenarios were considered with the following coverage mechanisms used in each:

- Both pitch-catch and pulse-echo sensing paths
- Sole pitch-catch sensing paths
- Sole pulse-echo sensing paths

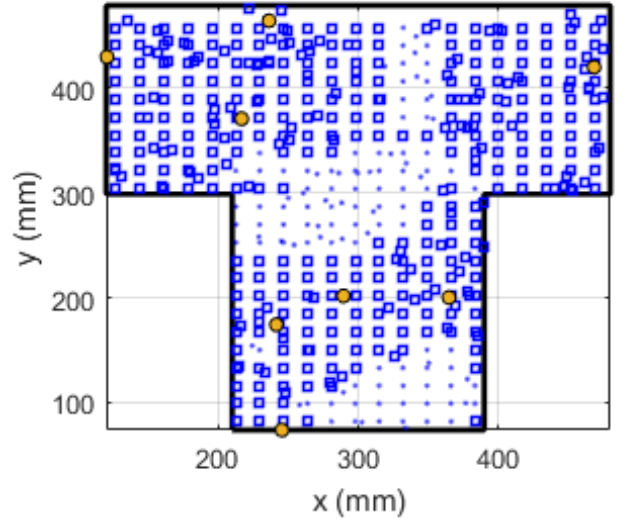
Figure 12 shows the results for the coverage scenarios that use sole pitch-catch and sole pulse-echo mechanisms for the four simulated cases. The optimized PZT wafer networks resulting from the proposed model are considered for the three coverage scenarios in order to be able to compare the results among each other for each simulated plate. For the square plate in Figure 12 a-b, the optimized PZT wafer network provided a coverage of 76% when using only pitch-catch mechanism as compared to 1.6% when using only pulse-echo mechanism. For the square plate with an opening in Figure 12 c-d, the scenarios using only pitch-catch and pulse-echo mechanisms resulted in a coverage of 70.2% and 5.4% respectively. This behavior is expected since the optimization model relied mainly on the pitch-catch sensing paths to localize PZT wafers because they cover a larger area as compared to the pulse-echo sensing path in

order to reduce the number of PZT wafers to the minimum. Thus, the placement of the PZT wafers were in favor of the pitch-catch method of detection. However, the control points that are near the edge of the plate are not covered by the pitch-catch configuration (Figure 12 a-c). By combining both mechanisms (Figure 11 b-d), the coverage increases to 96.4% for the square and 96% for the square plate with an opening. Thus, corner and edge control points became covered due to the summation of sensing paths from both pitch-catch and pulse-echo mechanisms which increased the level of coverage of this point to reach three or more after the combination. Here comes the value of considering the pulse-echo mechanism in the model. For the T-shaped plate in Figure 12 e-f, the coverage from the pitch-catch and pulse-echo mechanisms are 69.8% and 23% respectively; for the octagon plate, the coverages are 80.2% and 9% (Figure 12 g-h). The same behavior is encountered as well for these cases. Table 2 summarizes the coverage percentages for the simulated cases when using sole pitch-catch and sole pulse-echo mechanisms.

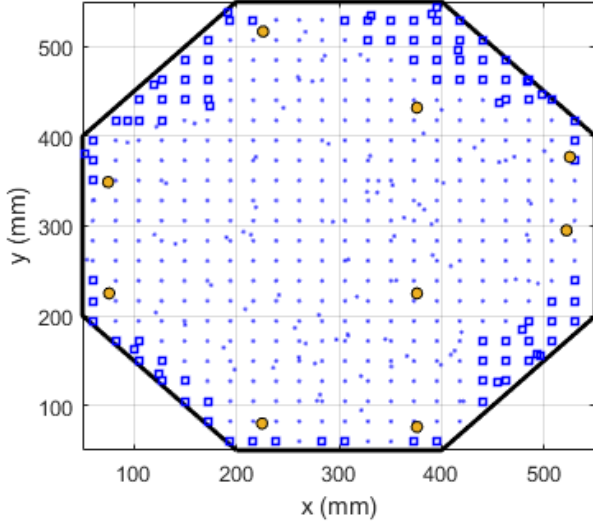




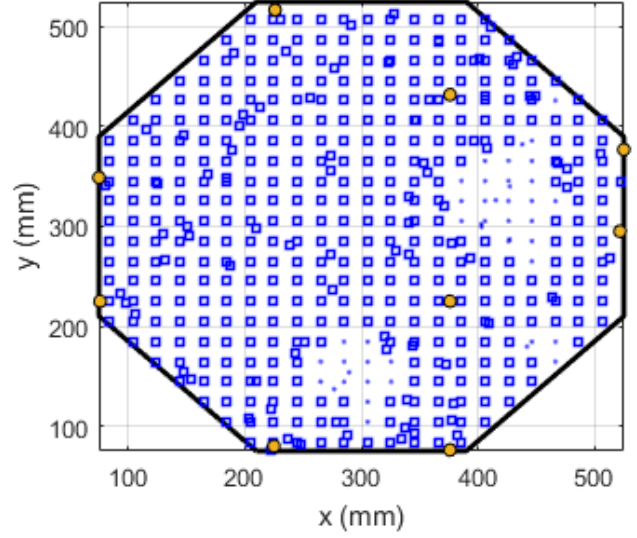
(e)



(f)



(g)



(h)

Figure 12. (a) Pitch-catch coverage for square plate, (b) pulse-echo coverage for square plate, (c) pitch-catch coverage for square plate with opening, (d) pulse-echo coverage for square plate with opening, (e) pitch-catch coverage for T-shaped plate, (f) pulse-echo coverage for T-shaped plate, (g) pitch-catch coverage for octagon plate, and (h) pulse-echo coverage for octagon plate

Table 2. Pitch-catch and pulse-echo coverage for simulated cases

Case	PZT wafers	Pitch-catch Coverage (%)	Pulse-echo Coverage (%)
Square	8	76	1.6
Square with opening	9	70.2	5.4
T-shape	8	69.8	23
Octagon	9	80.2	9

Moreover, a sensitivity analysis was conducted for the square plate with an opening in order to evaluate the importance of each PZT wafer which is later validated experimentally as well. Figure 13 (c) shows the optimized PZT wafer network considered with the number of each PZT wafer, and their corresponding x and y coordinates are summarized in Table 3. During each repetition, one PZT wafer is dropped, and the corresponding coverage percentage drop for the optimized PZT wafer network is determined while keeping the locations of all other PZT wafers constant. This is repeated for every single PZT wafer of the chosen case. The PZT that resulted in the highest drop in the coverage percentage is referred to as the most important sensor.

The coverage results are presented in Figure 13 (a) for the square plate with an opening. Figure 12 (b) shows the normalized importance of each PZT wafer calculated from the corresponding coverage percentages. The most important sensor is determined to be sensor 4 which resulted in the highest decrease of 25.5% in the coverage percentage. This result is expected since PZT wafer 4 is the one that migrated to the lower left corner and is the main reason behind the coverage of all the control points in that area. The sensing paths connected to PZT wafer 4 are the only ones covering that area (pitch-catch paths 4-1, 4-2, 4-3, 4-5, 4-6, and 4-7 and pulse-echo path of PZT wafer 4).

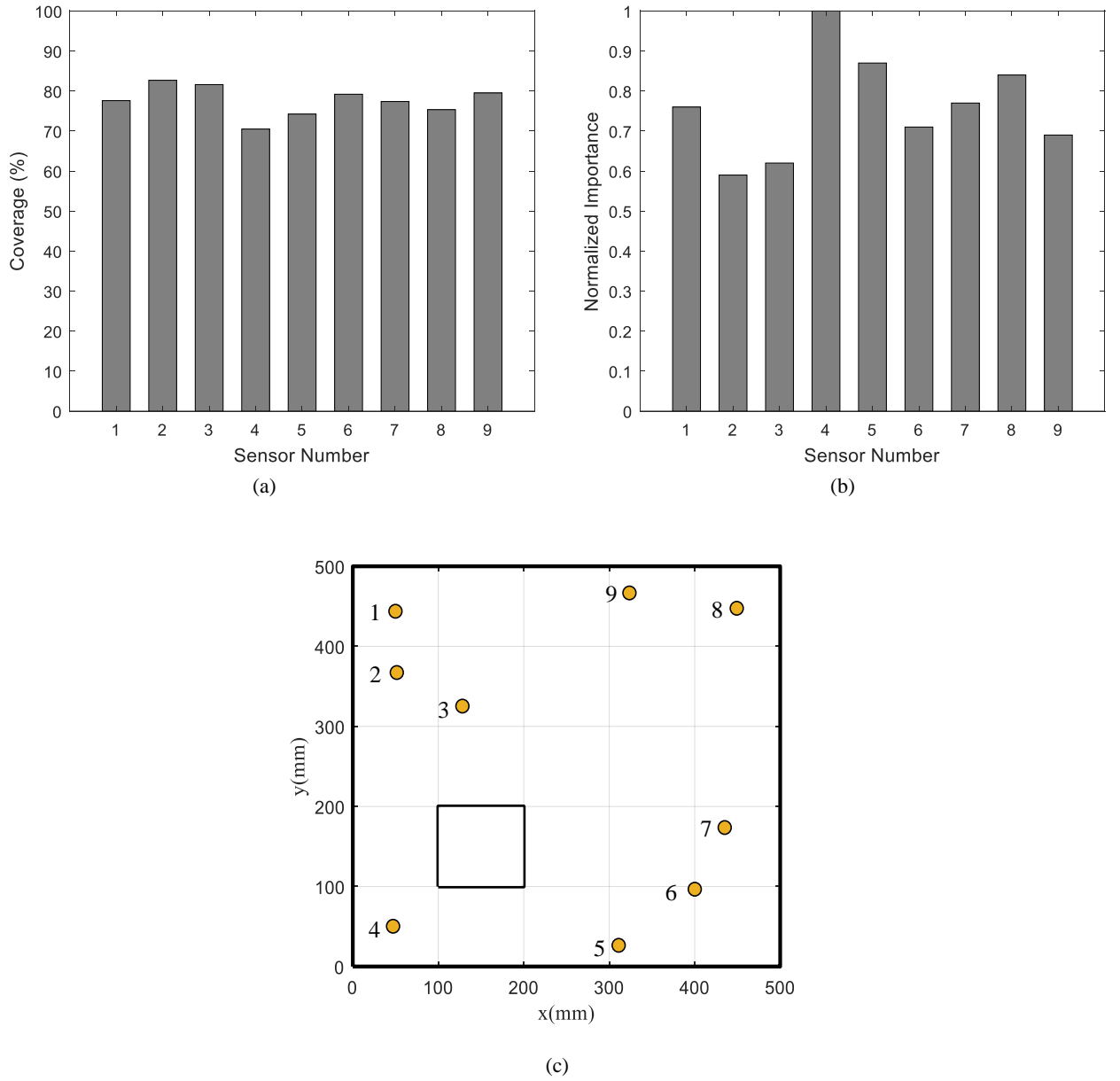


Figure 13. (a) Coverage after removing each PZT wafer, (b) the normalized importance of PZT wafers, and (c) optimized PZT wafer network for square plate with an opening

Table 3. Optimized locations of the PZT wafers

PZT Number	x-coordinate	y-coordinate
1	50.73	442.92
2	52.28	366.38
3	129.05	324.44
4	47.91	49.41
5	311.87	25.60
6	400.90	95.71
7	435.92	172.74
8	450.03	446.64
9	324.47	465.83

CHAPTER 5

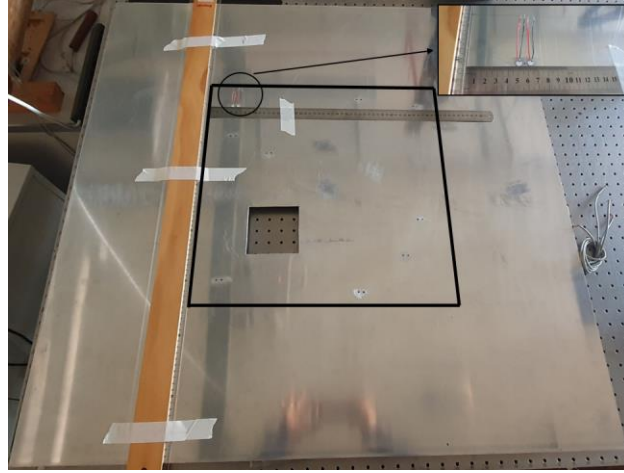
EXPERIMENTAL VALIDATION

The case of the square plate with an opening was implemented on an aluminum plate to further validate the model experimentally. Its main objective is to determine the effectiveness of the obtained optimized PZT wafer network in localizing a damage. This was achieved by evaluating the precision in damage localization after placing a simulated damage in different locations on the plate with the optimized network.

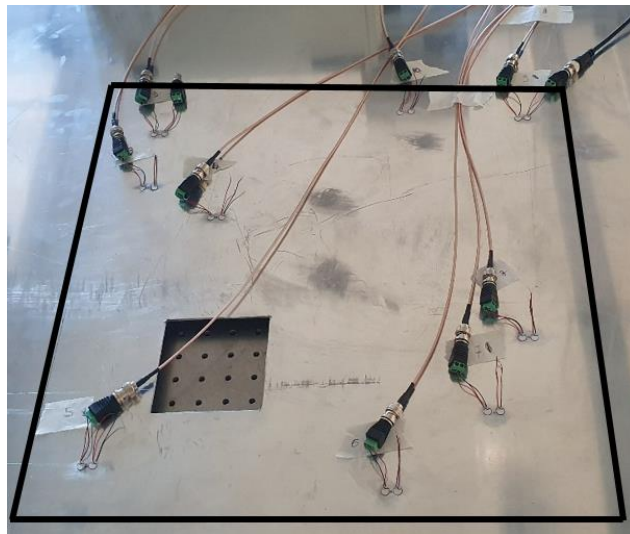
A. Experimental Setup

The same aluminum 1050 plate used previously was adjusted for this experimental validation. A $100 \times 100 \text{ mm}^2$ opening was introduced into the plate. Figure 14 (a) shows the bonding of the 9 PZT wafers to their corresponding coordinate locations as given by the optimized solution in Table 3. Due to hardware limitation, 18 PZT wafers were mounted on the plate as pairs to have one PZT acting as an actuator and the other as the receiving sensor to simulate the pulse-echo detection mechanism (Figure 14, b). The same experimental setup was used as the one described previously for the model parameters. The wave generator was used to generate bursts at an excitation frequency of 225 and 250 kHz. The signals generated were amplified to around 120 volts peak-to-peak voltage using the amplifier. When one PZT wafer is functioning as the actuator that generates the wave signal, all the other 9 PZTs (the one placed near it capturing reflection for pulse-echo and the other 8 PZTs working in pitch-catch) are acting as sensors that receives it. The role of the actuator was alternated among the 9 PZT pairs. The steel block was bonded to the plate at four different locations to act as the artificial damage. Refer to Figure 15 (e) for a schematic showing

these damage locations. For each damage case, this procedure was repeated to evaluate the precision in damage localization (Figure 15 a-b-c-d).

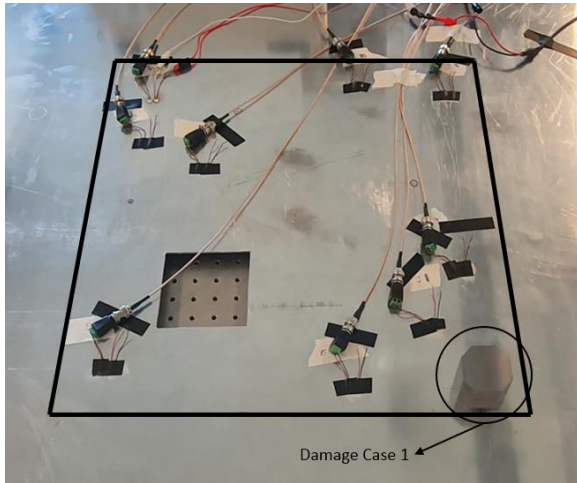


(a)

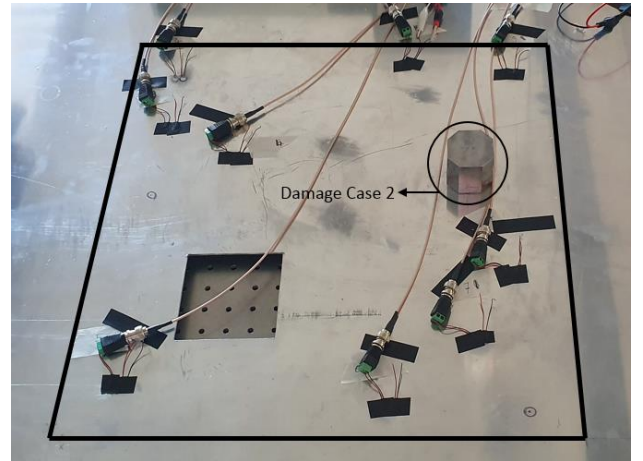


(b)

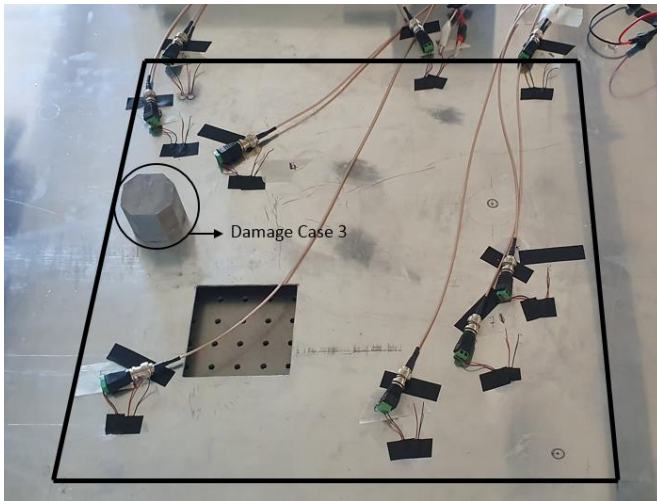
Figure 14. (a) Localizing the PZT wafers using the optimized coordinate results and (b) the optimized PZT wafer network of the square plate with an opening



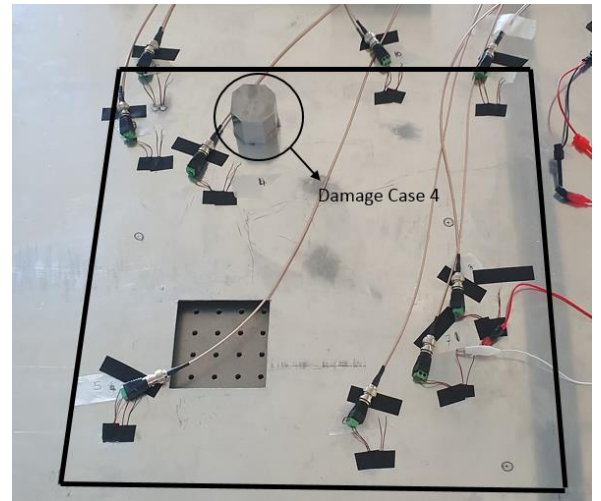
(a)



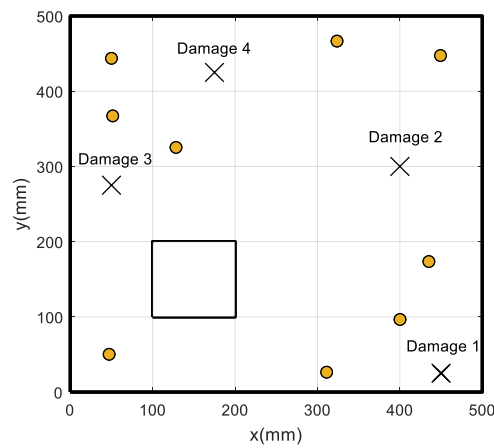
(b)



(c)



(d)



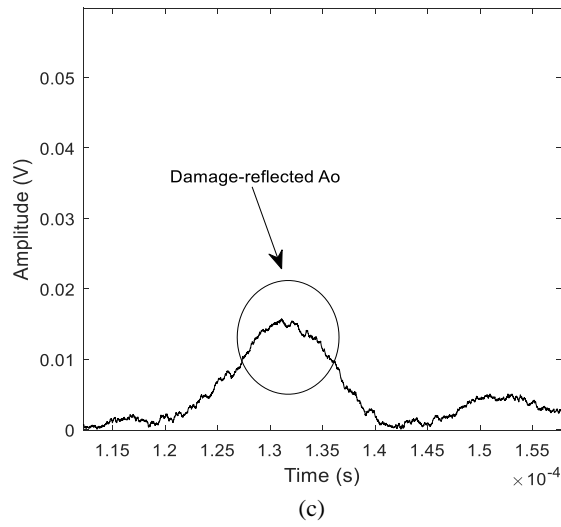
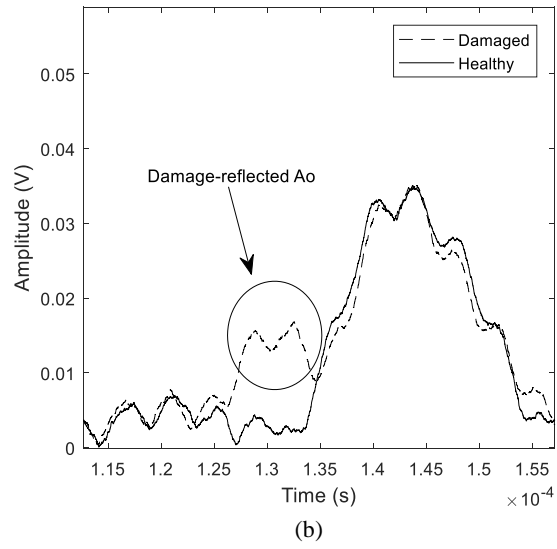
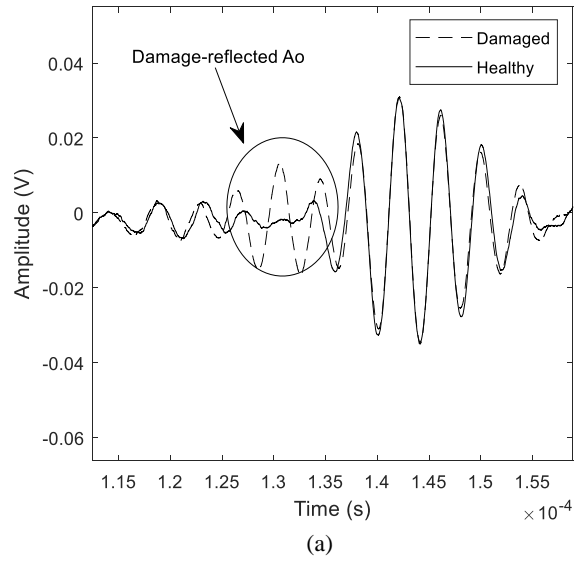
(e)

Figure 15. PZT wafer network with the damage placed according to damage case (a) 1, (b) 2, (c) 3, (d) 4, and (e) schematic showing the location of all damage cases

B. Signal Analysis

Before processing the collected data from the performed experiments and using them as inputs for the data fusion algorithm, an analysis of signals captured from both detection mechanisms is performed. This is done to determine which sensing paths are affected by the damage and to check the effect of the damage on the signals while comparing them to their healthy state.

Signals captured via a pulse-echo sensing path are shown in Figure 16. The healthy and damaged signals resulting from PZT wafer 6 when damage 2 is placed in the sensor network are represented in Figure 16 (a). This is the case of a sensing path that is passing through the damage and was able to detect it. In order to identify the reflection peak clearly, the Hilbert transform was applied for both signals in Figure 16 (b), and the difference between these two is shown in Figure 16 (c). The time at which the peak occurs for Figure 16 (c) is used to compute the damage locus which is discussed afterwards in equation 18. In brief, this reflection peak gives the potential distance between this PZT wafer and the damage after multiplying the time at which the peak occurred by the wave velocity. The fundamental order A_0 mode of the reflected signal is the one that is observed explicitly at the selected excitation frequency of 225 kHz. Thus, the A_0 mode is the one dominating over the S_0 mode which is suppressed. Figure 16 (d) shows the healthy and damaged pulse-echo signals for PZT wafer 1 which is far away from the damage. The pulse-echo sensing path is not affected by it; thus, no reflection peak is observed.



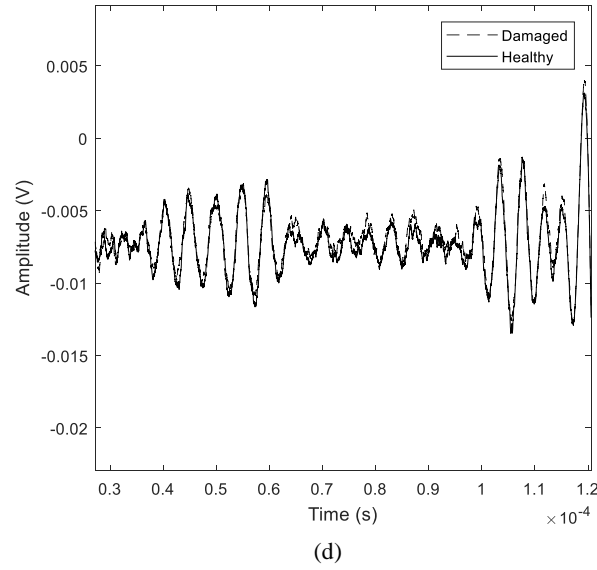


Figure 16. (a) Healthy and damaged signals resulting from pulse-echo sensing path of PZT wafer 6 for damage case 2, (b) Hilbert transform of the signals, (c) difference between the two signals, and (d) Healthy and damaged signals resulting from pulse-echo sensing path of PZT wafer 1

Signals captured via pitch-catch sensing paths are shown in Figure 17. The healthy and damaged signals resulting from the path covered by PZT wafers 7 and 9 when damage 2 is placed in the sensor network are represented in Figure 17 (a). The drop in the magnitude of the amplitude of the damaged signal is explicitly observed. Such a drop occurred since this path passes through the damage; thus, the signals captured from this sensing path were modulated by the damage. Figure 17 (b) represents the case of the sensing path 1-3 which does not pass by the damage. Thus, no drop was detected between the signals since they were not affected by it.

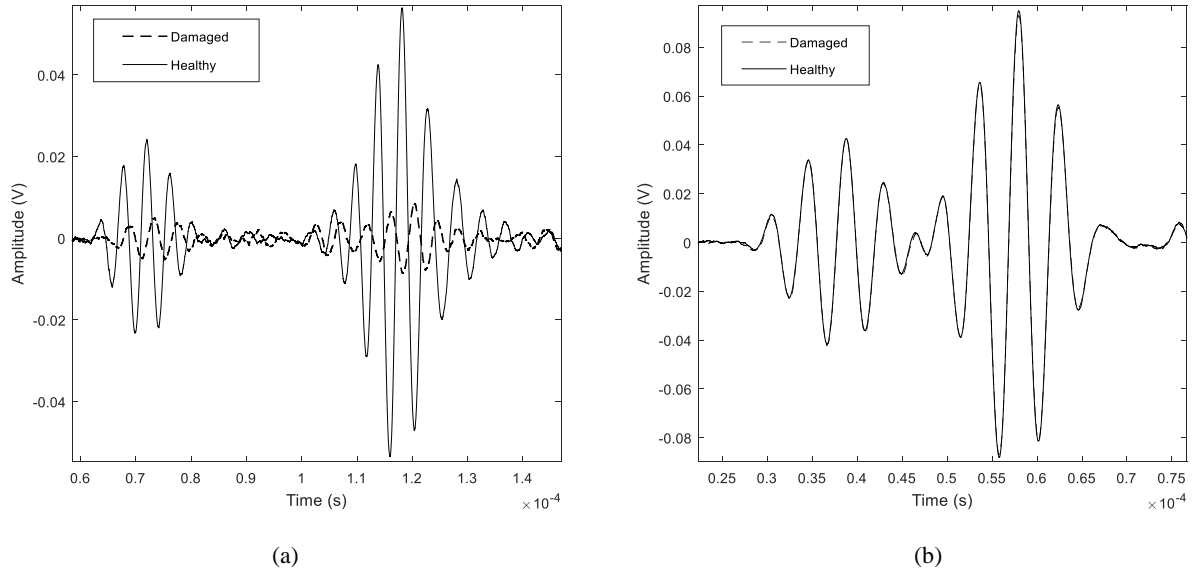


Figure 17. Healthy and damaged signals resulting from pitch-catch sensing path of PZT wafers (a) 7-9 and (b) 1-3 for damage case 2

C. Data Fusion and Damage Localization

Pitch-catch data fusion:

An anomaly value A_j ranging between 0 and 1 is assigned to each pitch-catch sensing path j . This parameter reflects the degree to which a sensing path is affected by the damage. These anomalies will be used to construct the damage image after fusing them with those coming from pulse-echo mechanism using a data fusion technique that is explained afterwards. The paths having higher anomalies are more likely to be near the damage. It is calculated by comparing the healthy signal (benchmark) to that of the damaged case according to the following equation:

$$A_j = 1 - \frac{\max(A_d)}{\max(A_h)} \quad (15)$$

where $\max(A_h)$ refers to the maximum amplitude of the healthy signal and $\max(A_d)$ refers to that of the damaged one. This anomaly is obtained for the remaining J sensing paths after reducing their number by half due to the dual function of PZTs, in

addition to removing those paths that are interrupted by a discontinuity, lie outside the geometry, or are collinear.

To construct the damage image, the area under analysis is divided into a uniform grid of 1 mm^2 , and each cell is assigned a probability of damage index (DI_{PC}) that reflects the existence of damage in this cell coming from pitch-catch sensing paths. It is obtained by merging the perceptions of the anomaly values from all the sensing paths. DI_{PC} is computed using equation (16) where $P_j(x, y)$ is the probability of damage at cell (x, y) for the j^{th} path. This probability is obtained by multiplying the anomaly measure A_j by the normal distribution function $f_j(z)$ for the j^{th} path. The possibility of the existence of a damage near a path is accounted by the influence of the anomaly value on the normal distribution. The shape of the normal distribution function (equation 17) was used to consider the maximum effect at the centerline of the path, and this effect decreases while moving away from the centerline on both sides. The mean μ is taken as zero since the perception of the damage location is higher along the centerline of the sensing path. In the experimental analysis performed to obtain the model parameters, it was found that the effect of a damage placed at a distance farther than 50 mm from a pitch-catch sensing path is negligible. Thus, the standard deviation was set to 50 mm for this analysis. The z value is the normal distance between the grid point and the centerline of the sensing path that is taken as a rectangular zone. This was considered to have the same damage effect for all grid points that are equidistant from the path centerline.

$$DI_{PC}(x, y) = \sum_{j=1}^J P_j(x, y) = \sum_{j=1}^J A_j f_j(z) \quad (16)$$

$$f(z) = \frac{1}{\sigma\sqrt{2\pi}} e^{-\frac{(z-\mu)^2}{2\sigma^2}} \text{ for } -\infty < z < +\infty \quad (17)$$

Pulse-echo data fusion:

In order to determine whether a damage is within the pulse-echo sensing path, the distance between the damage and the PZT wafer is calculated from the time of flight (ToF) of the wave signal (time for a wave to travel a certain distance). This distance is referred to as the damage locus for sensing path j (DL_j) and is computed as shown in equation 18. This locus is a prior perception of the damage location at one of the points lying on this circle. The velocity of the wave propagation (V) is considered to be constant before and after its interaction with the damage. The division by two is to account for the distance that the wave propagates from the PZT wafer to the damage and then back to the PZT wafer. For the paths that are far away from the damage, the damage locus is unavailable since no reflection peak will be detected for these signals as shown earlier in Figure 16 (d); thus, these paths will have no contribution in detecting the damage location. Theoretically, equation 18 results in damage loci for all effective paths that indicate the possible locations of damage.

$$DL_j = \frac{ToF \times V}{2} \quad (18)$$

A total of N pulse-echo sensing paths are available for a PZT wafer network with N PZTs. A DL is computed only for PZT wafers that are within an acceptable distance from the damage (paths showing reflection peaks). The area is meshed into a grid of 1 mm^2 as discussed earlier, and each cell is assigned a probability of damage index (DI_{PE}) that reflects the existence of damage in this cell. It considers fusing the probabilities of damage existence coming from every pulse-echo sensing path as shown in equation 19 where $f_j(z)$ is the normal distribution probability for the j^{th} path. The cells that are located on the damage loci have the highest probability of being the

corresponding damage location. As you move away from the locus from both sides, this probability decreases. To quantify these probabilities for all the cells, the normal distribution is used as presented in equation 17. The mean μ is taken as zero at the DL. In the experimental analysis performed to obtain the model parameters, it was found that a damage placed at a distance farther than 150 mm and smaller than 75 mm from a PZT wafer has a minor effect. Thus, the standard deviation was set to 75 mm (150 – 75 mm) for this analysis. The z value is the distance between the grid point and the damage locus of the corresponding pulse-echo sensing path. This was considered to have the same damage effect for all grid points that are equidistant from the DL of the considered sensing path.

$$DI_{PE}(x, y) = \sum_{j=1}^N f_j(z) \quad (19)$$

Fusing both mechanisms:

Since the magnitudes of the damage indices have no physical meaning, DI_{PC} and DI_{PE} were normalized for each grid point based on the maximum value of DI_{PC} and DI_{PE} respectively. Afterwards, the results of DI_{PC} and DI_{PE} were fused for each cell based on equation 20 in order to result in a damage index DI that estimates the presence of damage at this grid point taking into consideration all sensing paths (pitch-catch and pulse-echo). DI is again normalized based on the maximum DI across all grid points in order to result with values ranging between 0 and 1. The predicted damage is localized by searching for the control point with the highest damage index.

$$DI(x, y) = DI_{PC}(x, y) + DI_{PE}(x, y) \quad (20)$$

Note that a threshold was considered on the value of DI_{PC} . This is done since slight changes in the anomalies because of minor differences in the amplitudes of pitch-

catch signals might mislead the analysis. Amplitude differences less than a certain threshold are not a solid indication of the presence of damage near this sensing path. To consider the anomalies that have a real impact on the perception of damage, this threshold should be applied. In case the maximum of DI_{PC} was found to be less than this threshold, all the damage indices from pitch-catch sensing paths are disregarded from the analysis.

Another threshold was placed on the reflection peak of the pulse-echo sensing paths after subtracting the healthy signal from the damage one. This is also done to prevent the false interpretation of the presence of damage near the path when the reflection peak is low. In that manner, damage loci are calculated for signals with amplitudes above a certain threshold.

CHAPTER 6

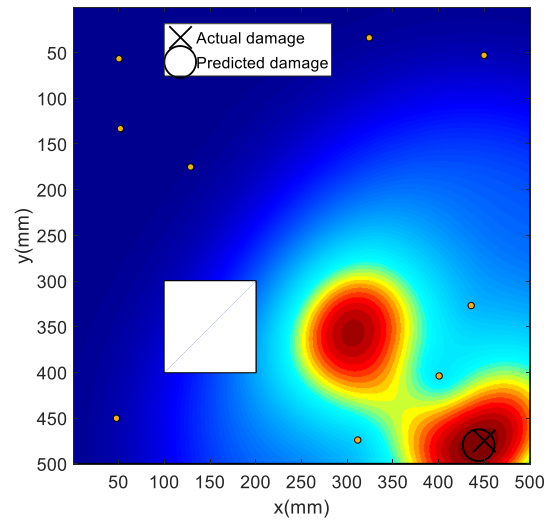
RESULTS AND DISCUSSION

A. Damage Detection and Localization

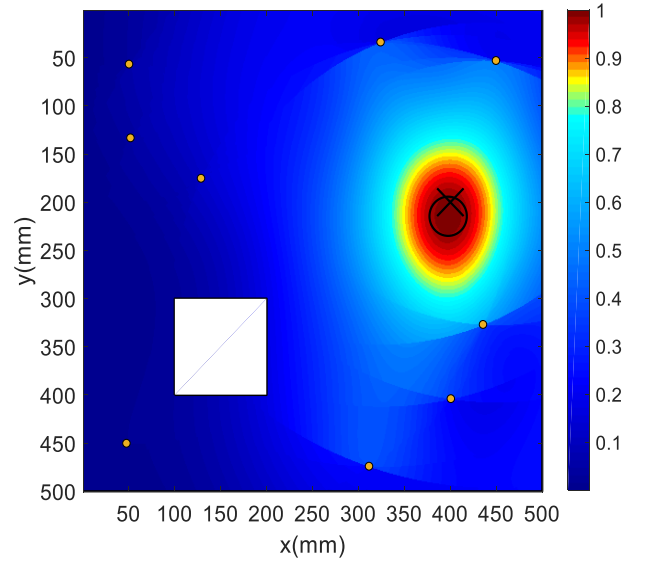
Four damage locations were considered to investigate the effectiveness in damage localization. Figure 18 summarizes the results obtained for each damage case using a frequency of 225 kHz. It is shown that the precision in detecting the damage location is high for all damage cases with a center distance of 2 mm between the actual and predicted damage. Damage localization is also investigated for a frequency of 250 kHz and showed high precision as well. All these results are summarized in Table 4, and the maximum distance for both frequencies did not exceed 16 mm.

Based on the optimized PZT wafer network and the data fusion technique used, a good detection was perceived for the damage despite its location within the area studied. It is interesting to note that damage 1 is placed in the corner where no pitch-catch sensing paths pass through it. Thus, it was fully covered by the pulse-echo sensing paths from the three PZT wafers located in the bottom right corner of the plate (Figure 18 (a)). The threshold considered helped in eliminating the effects of the pitch-catch sensing paths that would mislead the damage index perception by increasing the DI value for the grid points. Figure 18 (e) shows the PZT wafer network after removing two PZT elements (sensor 8 and 9) in order to investigate the damage detection for a damage placed in an uncovered area. After the PZT removal, the upper right area lost its coverage; thus, the location of damage 2 is now in an uncovered area. Figure 18 (f) shows that damage 2 was falsely detected after performing the data fusion. This shows

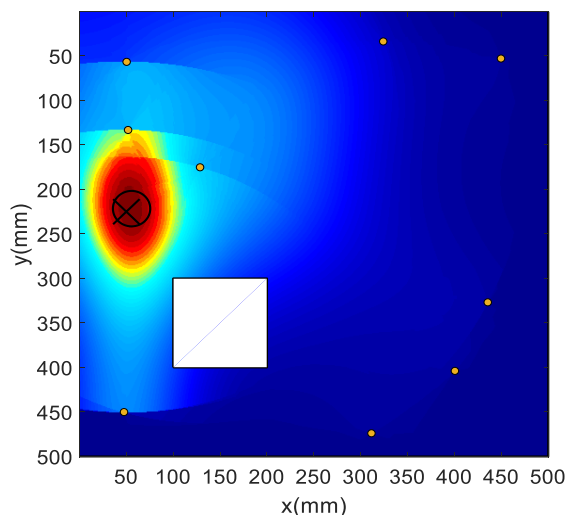
the effectiveness of the GA algorithm in enhancing the PZT wafer locations and in damage detection.



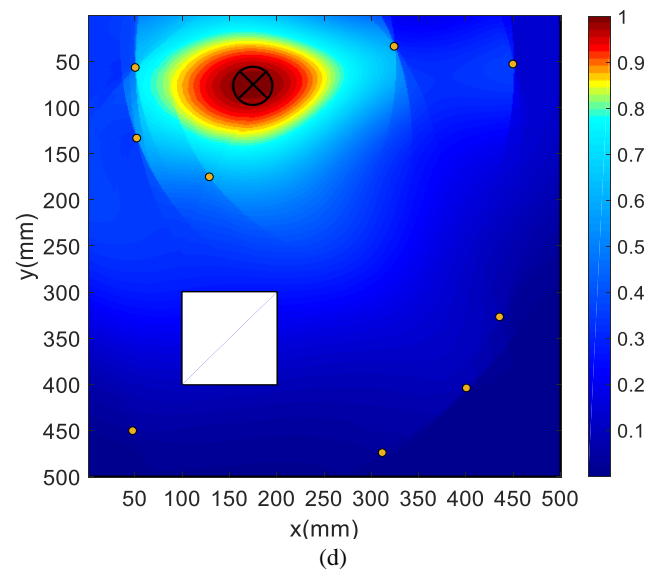
(a)



(b)



(c)



(d)

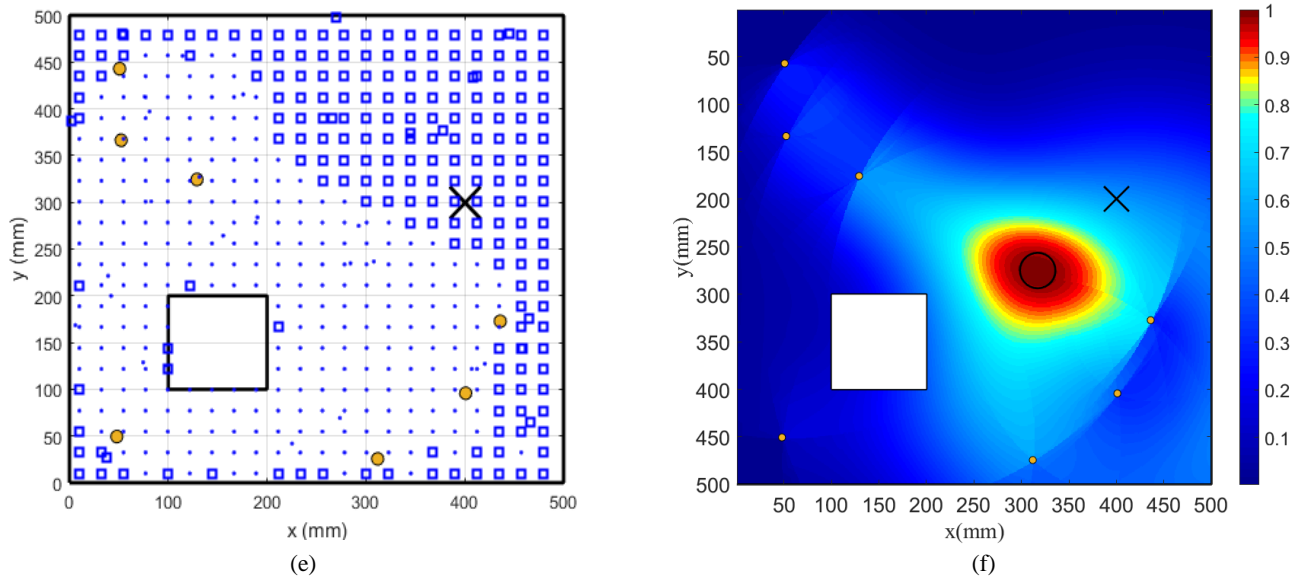


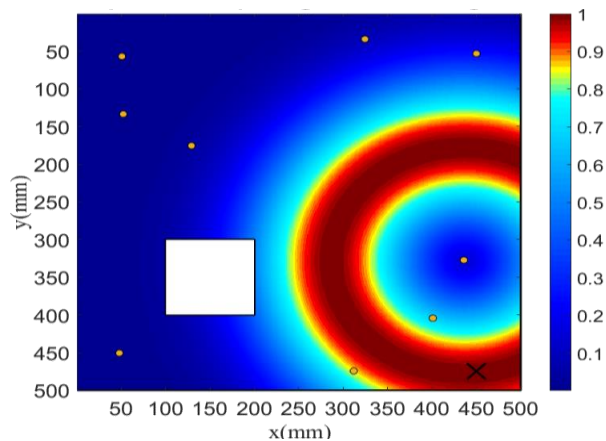
Figure 18. Damage localization on the square plate with an opening for (a) damage 1, (b) damage 2, (c) damage 3, (d) damage 4 of the optimized network, (e) the sensor network after removing some sensors, and (f) damage 2 of the network with missing sensors

Table 4. Damage scenarios and predicted locations using excitation frequencies of 225 and 250 kHz

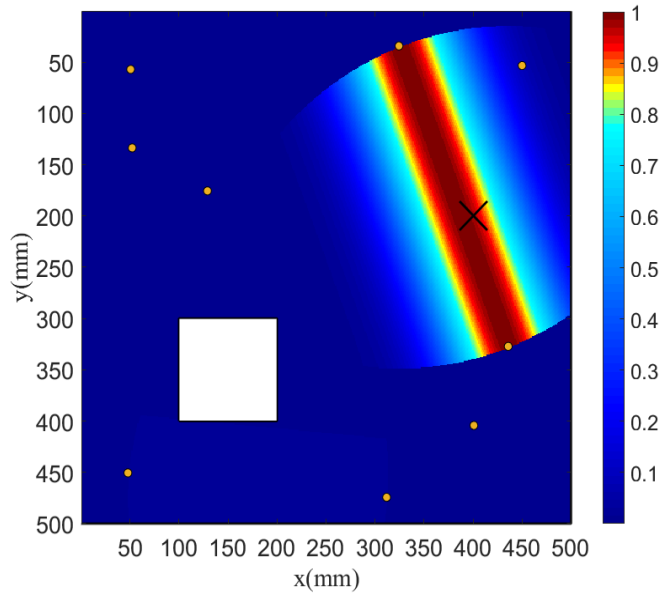
Sensor Network	Square with opening					
Excitation Frequency (kHz)	225			250		
Damage Location (mm)	Actual	Predicted	Variation	Actual	Predicted	Variation
Damage 1	(450, 475)	(444, 480)	7.81	(450, 475)	(440, 477)	10.20
Damage 2	(400, 200)	(398, 215)	15.13	(400, 200)	(399, 213)	13.04
Damage 3	(50, 225)	(56, 222)	6.71	(50, 225)	(48, 229)	4.47
Damage 4	(175, 75)	(175, 77)	2.00	(175, 75)	(181, 70)	7.81

B. Single Sensing Path Analysis

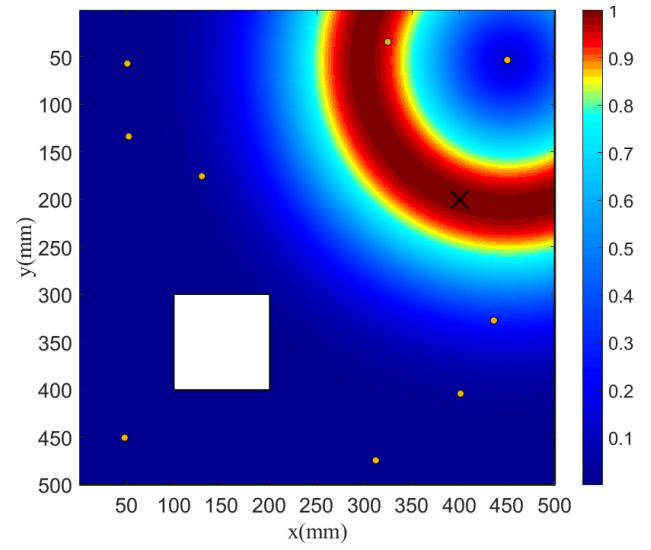
Figure 19 summarizes single pitch-catch and pulse-echo sensing paths for all damage cases. These help in demonstrating the contribution of sensing paths in damage localization. Figure 19 (a, c, e, g) show a single pulse-echo sensing path. The grid points lying on the circle having the PZT as the center and the distance between the damage and the PZT as its radius have the highest perception for the presence of damage (darkest red area). Moving away from this damage locus, the perception of damage decreases gradually. For the pitch-catch sensing path, Figure 19 (d) shows two paths (path 1-4 and 1-7) for damage case 3. For path 1-4 which passes through the damage, the grid points within this path show high DI's with those lying on the centerline of the path having the highest values (highest perception of damage). This effect decreases as the distance between the grid point and the centerline increases. In addition, path 1-7 showed lower values since this path is far away from the damage. Thus, the difference between the amplitudes of the healthy and damaged signals was mild resulting in a low anomaly value which therefore leads to a low damage index. Similar behavior can be seen in Figure 19 (b and f) for damage cases 2 and 4 respectively.



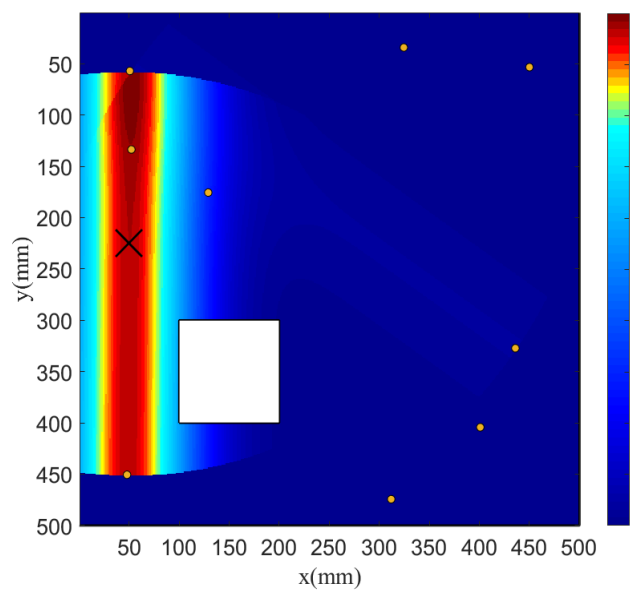
(a)



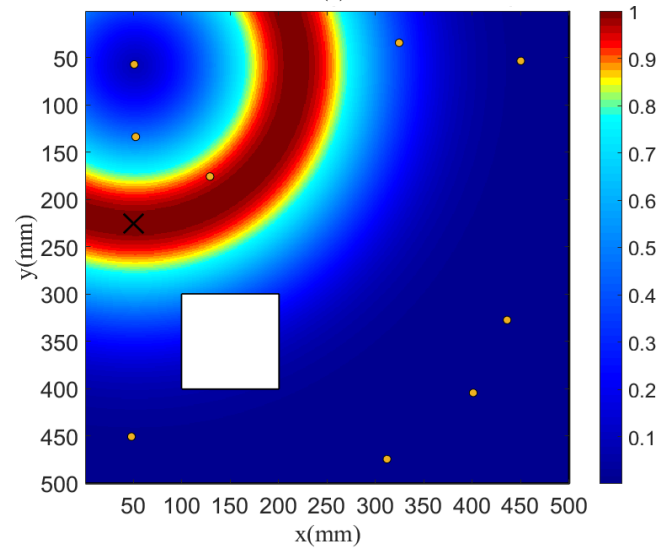
(b)



(c)



(d)



(e)

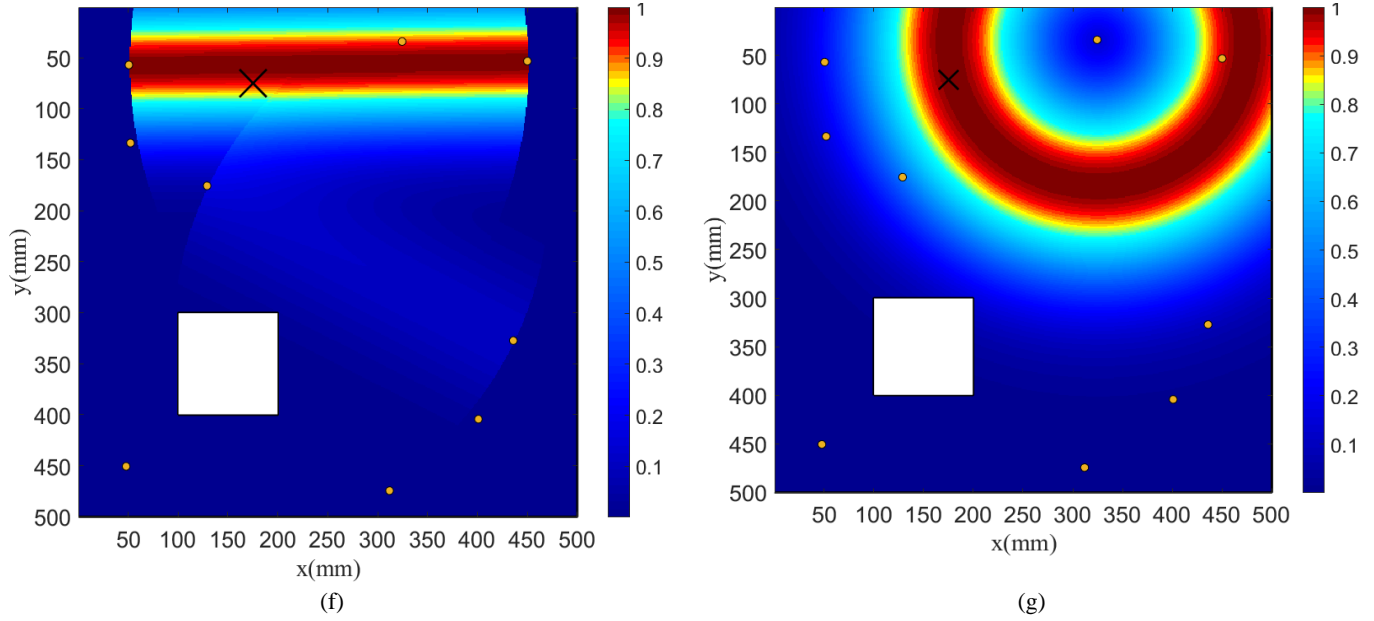


Figure 19. (a) PZT 7 pulse-echo sensing path for damage 1, (b) 7-9 pitch-catch sensing path for damage 2, (c) PZT 8 pulse-echo sensing path for damage 2, (d) 1-4 pitch-catch sensing path for damage 3, (e) PZT 1 pulse-echo sensing path for damage 3, (f) 1-8 pitch-catch sensing path for damage 4, and (g) PZT 9 pulse-echo sensing path for damage 4

In general, the proposed model was proved to be efficient in finding the optimal sensor network that could be applied in different applications. For the data fusion algorithm, it can be used in systems that considers both the pitch-catch and the pulse-echo detection mechanism or either one. When larger and more complex systems are considered, this will result in the need of more PZT wafers and control points to provide a satisfactory coverage at the expense of an increase in the computation time. Each mechanism is more efficient in plates whose geometries resemble their sensing path shapes. For the pitch-catch configuration, it is more efficient with geometries closer to rectangular shapes. For the pulse-echo configuration, it is more efficient with geometries resembling the circular coverage behavior. However, the advantage is that both mechanisms complement each other. Pitch-catch paths provide larger coverage areas resulting in the use of less PZT wafers in the optimal network. On the other side,

pulse-echo paths show a major advantage in covering areas where pitch-catch paths could not reach such as corners and edges. Thus, combining both mechanisms provide higher coverage of the area studied using the same PZT wafer network. One of the limitations of this study is the model's automatic assumption that every PZT wafer provides coverage through both mechanisms instead of letting the model determine which one is effective to use in this area. Another limitation is the use of parameters that are material specific to Aluminum 1050. These parameters that were determined through experimentation are used as inputs to the model.

CHAPTER 7

CONCLUIONS

This paper has presented an advanced method that optimizes the PZT wafer locations within a network using GA. Two mechanisms of detection were implemented in the model which are coverage through pulse-echo and pitch-catch sensing paths. The objective function focused on maximizing the coverage of control points while minimizing the number of PZT wafers used. The sensing path parameters for pitch-catch (path coverage and maximum spacing) and pulse-echo (reflection coverage) were determined through experimentation on an aluminum plate.

Simulated cases were optimized for plates with different geometries and have shown great improvements in the coverage of the area studied as compared to coverage provided by the preliminary PZT wafer networks. For the same minimized number of PZT wafers, the model could reallocate the PZT wafers to meet the coverage requirements (95% and higher). Furthermore, investigating the coverage of sole pitch-catch and sole pulse-echo detection mechanisms for all the simulated cases with the optimized PZT wafer network proved the effectiveness of combining both mechanisms together to increase the coverage percentage and to provide coverage for points located near edges and corners.

Moreover, experimental validation proved the benefits of the optimization model in localizing damages precisely. Artificial damage was placed within the network and was detected with high precision reaching a maximal error of 3% of the maximal distance in the geometry using excitation frequencies of 225 and 250 kHz.

Future work is proposed to generalize the model further and allow it to determine which detection mechanism is required by each PZT wafer instead of automatically assuming the use of both.

REFERENCES

1. Derriso, M., et al. Integrated vehicle health management: the key to future aerospace systems. in Proceedings of the Fourth International Workshop on Structural Health Monitoring. 2003.
2. Speckmann, H. and J.-P. Daniel. Structural health monitoring for airliner, from research to user requirements, a European view. in CANEUS 2004 Conference on Micro-Nano-Technologies. 2004.
3. Markmiller, J.F. and F.-K. Chang, Sensor network optimization for a passive sensing impact detection technique. Structural Health Monitoring, 2010. 9(1): p. 25-39.
4. Zhou, C., Z. Su, and L. Cheng, Probability-based diagnostic imaging using hybrid features extracted from ultrasonic Lamb wave signals. Smart Materials and Structures, 2011. 20(12): p. 125005.
5. Ryles, M., et al., Comparative study of nonlinear acoustic and Lamb wave techniques for fatigue crack detection in metallic structures. Fatigue & Fracture of Engineering Materials & Structures, 2008. 31(8): p. 674-683.
6. Sohn, H. and S.J. Lee, Lamb wave tuning curve calibration for surface-bonded piezoelectric transducers. Smart Materials and Structures, 2009. 19(1): p. 015007.
7. Su, Z. and L. Ye, Identification of damage using Lamb waves: from fundamentals to applications. Vol. 48. 2009: Springer Science & Business Media.
8. Raghavan, A., Guided-wave structural health monitoring. 2007.

9. Sharif-Khodaei, Z., M. Ghajari, and M. Aliabadi, Determination of impact location on composite stiffened panels. *Smart Materials and Structures*, 2012. 21(10): p. 105026.
10. Ghajari, M., et al., Identification of impact force for smart composite stiffened panels. *Smart Materials and Structures*, 2013. 22(8): p. 085014.
11. Gresil, M., A. Muller, and C. Soutis. Acousto-ultrasonic Structural Health Monitoring of aerospace composite materials. in *Emerging Technologies in Non-Destructive Testing VI: Proceedings of the 6th International Conference on Emerging Technologies in Non-Destructive Testing (Brussels, Belgium, 27-29 May 2015)*. 2015. CRC Press.
12. Chang, F.-K. and F. Kopsaftopoulos, *Structural health monitoring 2015: system reliability for verification and implementation*. 2015: DEStech Publications, Inc.
13. Yi, T.H., H.N. Li, and M. Gu, Optimal sensor placement for structural health monitoring based on multiple optimization strategies. *The Structural Design of Tall and Special Buildings*, 2011. 20(7): p. 881-900.
14. Tarhini, H., et al., Optimization of piezoelectric wafer placement for structural health-monitoring applications. *Journal of Intelligent Material Systems and Structures*, 2018. 29(19): p. 3758-3773.
15. Thiene, M., Z.S. Khodaei, and M. Aliabadi, Optimal sensor placement for maximum area coverage (MAC) for damage localization in composite structures. *Smart materials and structures*, 2016. 25(9): p. 095037.
16. Salmanpour, M., Z. Sharif Khodaei, and M. Aliabadi, Transducer placement optimisation scheme for a delay and sum damage detection algorithm. *Structural Control and Health Monitoring*, 2017. 24(4): p. e1898.

17. Zhou, C., Z. Su, and L. Cheng, Quantitative evaluation of orientation-specific damage using elastic waves and probability-based diagnostic imaging. *Mechanical Systems and Signal Processing*, 2011. 25(6): p. 2135-2156.
18. Wang, D., et al., Probabilistic Damage Identification Based on Correlation Analysis Using Guided Wave Signals in Aluminum Plates. *Structural Health Monitoring*, 2010. 9(2): p. 133-144.
19. Wu, Z., et al., Validation and evaluation of damage identification using probability-based diagnostic imaging on a stiffened composite panel. *Journal of Intelligent Material Systems and Structures*, 2015. 26(16): p. 2181-2195.
20. Worden, K. and A. Burrows, Optimal sensor placement for fault detection. *Engineering structures*, 2001. 23(8): p. 885-901.
21. Mallardo, V., M. Aliabadi, and Z.S. Khodaei, Optimal sensor positioning for impact localization in smart composite panels. *Journal of intelligent material systems and structures*, 2013. 24(5): p. 559-573.
22. Mallardo, V. and M. Aliabadi, Optimal sensor placement for structural, damage and impact identification: A review. *Struct. Durab. Health Monit*, 2013. 9: p. 287-323.
23. Jarmer, G. and S. Kessler, Probability of detection assessment of a guided wave structural health monitoring system. *Structural Health Monitoring* 2015, 2015.
24. Flynn, E.B. and M.D. Todd, A Bayesian approach to optimal sensor placement for structural health monitoring with application to active sensing. *Mechanical Systems and Signal Processing*, 2010. 24(4): p. 891-903.

25. Flynn, E.B. and M.D. Todd, Optimal placement of piezoelectric actuators and sensors for detecting damage in plate structures. *Journal of Intelligent Material Systems and Structures*, 2010. 21(3): p. 265-274.
26. Staszewski, W.J. and K. Worden. Overview of optimal sensor location methods for damage detection. in *Smart Structures and Materials 2001: Modeling, Signal Processing, and Control in Smart Structures*. 2001. International Society for Optics and Photonics.
27. Guo, H., et al., Optimal placement of sensors for structural health monitoring using improved genetic algorithms. *Smart materials and structures*, 2004. 13(3): p. 528.
28. Sun, X., G. Hou, and Z. Wang. Sensitivity-based optimal sensor placement of multi-type sensor. in *Health Monitoring of Structural and Biological Systems 2013*. 2013. International Society for Optics and Photonics.
29. Croxford, A.J., P.D. Wilcox, and B.W. Drinkwater. Quantification of sensor geometry performance for guided wave SHM. in *Health Monitoring of Structural and Biological Systems 2009*. 2009. International Society for Optics and Photonics.
30. Wandowski, T., P. Malinowski, and W. Ostachowicz, Damage detection with concentrated configurations of piezoelectric transducers. *Smart Materials and Structures*, 2011. 20(2): p. 025002.
31. Malinowski, P., T. Wandowski, and W. Ostachowicz, Damage detection potential of a triangular piezoelectric configuration. *Mechanical Systems and Signal Processing*, 2011. 25(7): p. 2722-2732.

32. Rosalie, C., et al., Structural health monitoring of composite structures using stress wave methods. *Composite Structures*, 2005. 67(2): p. 157-166.
33. McKeon, J.C. and M.K. Hinders, Parallel projection and crosshole Lamb wave contact scanning tomography. *The Journal of the Acoustical Society of America*, 1999. 106(5): p. 2568-2577.
34. Su, Z., et al., On selection of data fusion schemes for structural damage evaluation. *Structural health monitoring*, 2009. 8(3): p. 223-241.
35. Su, Z., et al., Predicting delamination of composite laminates using an imaging approach. *Smart Materials and Structures*, 2009. 18(7): p. 074002.
36. Tua, P., S. Quek, and Q. Wang, Detection of cracks in cylindrical pipes and plates using piezo-actuated Lamb waves. *Smart materials and structures*, 2005. 14(6): p. 1325.
37. Michaels, J.E. and T.E. Michaels, Guided wave signal processing and image fusion for in situ damage localization in plates. *Wave motion*, 2007. 44(6): p. 482-492.
38. Lee, B. and W. Staszewski, Sensor location studies for damage detection with Lamb waves. *Smart materials and structures*, 2007. 16(2): p. 399.
39. Fendzi, C., et al., Optimal sensors placement to enhance damage detection in composite plates. 2014.
40. Ismail, Z., et al., Sensor placement optimization on complex and large metallic and composite structures. *Structural Health Monitoring*, 2020. 19(1): p. 262-280.
41. Huang, C.-F. and Y.-C. Tseng, The coverage problem in a wireless sensor network. *Mobile networks and Applications*, 2005. 10(4): p. 519-528.

42. Dini, G., et al., Generation of optimized assembly sequences using genetic algorithms. *CIRP Annals*, 1999. 48(1): p. 17-20.
43. Houck, C.R., J. Joines, and M.G. Kay, A genetic algorithm for function optimization: a Matlab implementation. *Ncsu-ie tr*, 1995. 95(09): p. 1-10.